Journal of Materials Chemistry A

ROYAL SOCIETY OF CHEMISTRY

PAPER

View Article Online
View Journal | View Issue

Cite this: J. Mater. Chem. A, 2026, 14, 14224

Defect engineering and triangular copper as key drivers for ultralow thermal conductivity in Cu_2ZrS_3 polytypes

Lucas Le Gars, *[a] Sakshi Verma, [b] Minati Tiadi,[a] Carmelo Prestipino, *[a] Animesh Das,[b] Bin Zhang,[cd] Olivier Perez,[a] Philippe Boullay, [a] Denis Menut, [e] Bernard Raveau, [a] Gaëlle Riou,[a] Adèle Renaud, [f] Kanishka Biswas, [b] Umesh V. Waghmare, [b] Xiaoyuan Zhou, [cd] Koichiro Suekuni [g] and Emmanuel Guilmeau *[a]

Copper-rich sulfides are promising materials for energy-conversion applications due to their environmental compatibility, cost-effectiveness, and earth abundance. Their structural diversity and chemical flexibility offer a fantastic playground for the discovery of new structures and compounds with various properties. We demonstrate that the presence of triangular copper in the ordered CdI_2-type $Zr_{2/3}Cu_{1/3}S_2$ layers of Cu_2ZrS_3 induces a high potential for polytypism in this sulfide. Two new layered polytypes, *P*31*c*(ABCB) and *R*3(ABC), are synthesized. Based on a comprehensive analysis by single-crystal X-ray diffraction, 3D ED and HRSTEM analyses, we highlight that these polytypes differ in their stacking sequences while sharing identical tetrahedral copper layers and ordered $Zr_{2/3}Cu_{1/3}S_2$ layers. Both polytypes are characterized by large anisotropic vibrations of copper in triangular coordination. Low-temperature heat capacity and Raman spectroscopy, supported by phonon calculations, identify low-energy optical phonons associated with Cu atoms, which couple strongly to acoustic modes, yielding non-Debye behavior and extremely short phonon lifetimes. The *R*3 polytype displays intrinsically ultralow lattice thermal conductivity, reaching 0.35 W m^{-1} K^{-1} at 673 K, among the lowest reported in sulfides. Our findings provide new insights into the complex crystal chemistry and polytypism of copper-rich sulfides in relation to vibrational properties, opening new perspectives for the exploration of these materials.

Received 10th December 2025
Accepted 10th February 2026

DOI: 10.1039/d5ta10102f

rsc.li/materials-a

Introduction

Heat propagates through a solid primarily *via* electrons or lattice vibrations.[1,2] In crystalline electrical insulators, where the electronic contribution to thermal conductivity, κ_e, is negligible, phonons become the dominant carriers of thermal energy.[3] Understanding thermal transport in such materials remains a fundamental challenge, as it involves complex many-body interactions at both structural, nano- and microscopic levels. This has spurred significant interest in analyzing lattice thermal conductivity, κ_L, in relation to crystal structure features and chemical bonding.[4] The ability to control κ_L is indeed crucial for a wide range of applications. While materials with high κ_L are crucial for applications such as heat dissipation in electronics and thermal energy transmission,[5] low κ_L is required for technologies like thermal barrier coatings, hot phonon bottlenecks in photovoltaics, and thermoelectrics.[6–8]

The search for optimized thermoelectric materials with low κ_L poses an interesting conundrum because of the delicate balance that must be achieved between charge and thermal transport. Extrinsic phonon scattering approaches have been widely developed, such as alloying, grain boundary engineering, mesoscale structuring, and nanostructuring, which work by introducing point defects and creating nano-precipitates and interfaces that effectively scatter phonons and suppress thermal conductivity. Another approach and challenge consists in developing materials where intrinsic phonon–phonon interactions within the crystal structure generate phonon scattering and intrinsic low lattice thermal conductivity, while preserving high power factors. Low κ_L in crystalline solids can be achieved, for example, in complex crystal structures,[9] rattling in caged

[a]CRISMAT, CNRS, Normandie Univ, ENSICAEN, Unicaen, 14000 Caen, France. E-mail: lucas.le-gars@ensicaen.fr; carmelo.prestipino@ensicaen.fr; emmanuel.guilmeau@ensicaen.fr

[b]Jawaharlal Nehru Centre for Advanced Scientific Research (JNCASR), Jakkur, Bengaluru, Karnataka, India

[c]College of Physics and Institute of Advanced Interdisciplinary Studies, Chongqing University, Chongqing 401331, China

[d]Analytical and Testing Center of Chongqing University, Chongqing 401331, China

[e]Ligne MARS, L'Orme des Merisiers, Synchrotron SOLEIL, 91192 Saint-Aubin, Gif-sur-Yvette, France

[f]Univ. Rennes, CNRS, ISCR – UMR 6226, F-35000 Rennes, France

[g]Interdisciplinary Graduate School of Engineering Sciences, Kyushu University, 6-1 Kasugakouen, Kasuga, Fukuoka 816-8580, Japan

structures,[10–13] anisotropic cationic vibrations,[14–17] incipient ionic conductivity,[18] correlated rattling of one-dimensional atomic chains,[19] resonant bonding,[20] low dimensionality,[20–24] anharmonicity and weak bonding[25] in relation (or not) to the stereo-chemical activity of lone pairs,[26–30] and ferroelectric instability.[31] These strategies have been especially studied in heavy metal selenides and tellurides over the last few decades. Nevertheless, selenides and tellurides, while offering excellent thermoelectric performances, fall outside the category of sustainable materials. With an overall abundance of 4 to 5 orders of magnitude greater than Se or Te, sulfur is a much more desirable substitute.[32] Metal sulfides indeed have significant advantages, for most of them, of being inexpensive, abundant, non-toxic, and ensuring long-term price stability and availability. However, the main drawback of sulfides is that they generally exhibit higher κ_L, due to the lighter atomic weight of sulfur compared to selenium or tellurium. This has driven considerable efforts from the thermoelectric community in the last decade to develop sulfide-based materials with ultralow κ_L.[33–35] As shown in Fig. 1, it includes Sn- and Bi-based compounds characterized by low structural dimensionality and weak bonding due to the stereochemical activity of their lone pairs (*e.g.*, SnS,[36] Bi_2S_3,[37] $CuPbBi_5S_9$,[38] $PbBi_2S_4$,[39] and $PbSnS_2$ (ref. 40)), Sn-based colusites with structural disorder,[41,42] and structures with large anisotropic atomic vibrations (*e.g.*, Cu_3BiS_3,[43] $Cu_4Sn_7S_{16}$,[44] and tetrahedrite[45]). The three-fold coordination of copper is the key factor for large anisotropic vibrations in the structure and consequently is a trump for the appearance of ultra-low thermal conductivity.

In this context, Z. Li *et al.*[46] recently reported an intrinsically low lattice thermal conductivity of 0.35 W m^{-1} K^{-1} at 683 K in the new compound of bi-dimensional character Cu_2ZrS_3. The unique structural feature of this compound is based on the existence of Cu in an axially distorted triangular coordination, which, according to the authors, leads to pronounced lattice anharmonicity and low lattice thermal conductivity.

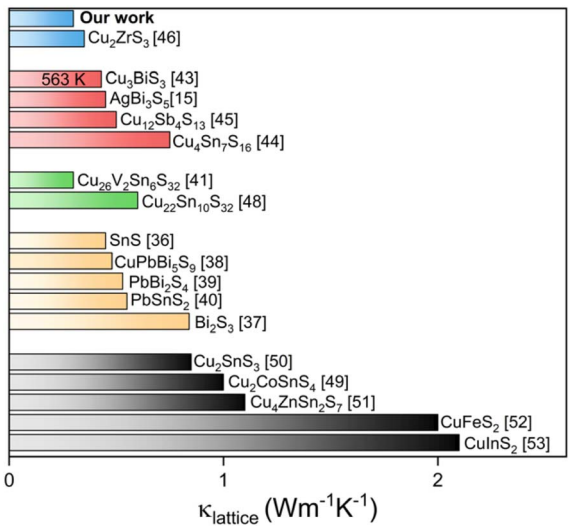

Fig. 1 Lattice thermal conductivity, at 700 K, in state-of-the-art thermoelectric polycrystalline sulfides.[15,36–41,43–53]

Interestingly, the supplementary information of this study shows powder diffraction patterns of alternative samples synthesized with different thermal histories. The patterns, although showing a good resemblance, slightly differ in the number of peaks and intensity ratio. This observation has drawn our attention and motivated us to investigate the relationship between synthesis parameters, structure, microstructure, thermal and vibrational properties of Cu_2ZrS_3. Our study reveals that the formation of two new structural polytypes is driven by the synthesis conditions, with significant differences both at the structural and microscopic levels, including distinct stacking arrangements and structural defects of different natures. The combination of heat capacity (C_p) fitting, Raman spectroscopy analysis and phonon calculations further confirms the existence of Cu associated low-energy optical phonons, enabling pronounced interactions between optical and acoustic modes, leading to ultra-low thermal conductivity. Based on both experimental approaches and computational modelling, our findings provide in-depth insights into the relationship between the crystal structure and thermal transport properties of layered metal sulfides, and open new perspectives for the exploration of cost-effective and sustainable sulfide compounds for thermal management applications.

Experimental section

Synthesis

Cu_2ZrS_3 powders were synthesized by a two-step solid state reaction in evacuated silica tubes from the precursors (Cu (99%, Alfa Aesar), Zr (99.5%, sponge, Alfa Aesar), and S (99.5%, Alfa Aesar). All sample preparations and handling of powders were performed in an argon filled glovebox with oxygen content below 1 ppm. Cu, Zr, and S were mixed in an agate mortar with the appropriate stoichiometric ratio, sealed in an evacuated silica tube, and heated to 1373 K at a rate of 50 K h^{-1}. The powder was held at that temperature for 48 hours, followed by two different cooling processes. (1) In the first approach, the 48-hour temperature plateau was followed by rapid quenching in open air. The resulting powder was then ground and subjected to the same heat treatment again. (2) In the second approach, the sample was slowly cooled down to room temperature at a rate of 50 K h^{-1}. The resulting Cu_2ZrS_3 powder was then crushed and compacted for a second firing under the same conditions.

In both cases, the obtained sample was once again ground and sieved down to 200 μm to remove large agglomerates. The powders were then placed in a graphite die of 10 mm diameter and densified by SPS (FCT HPD 25) at 873 K for 30 min under a pressure of 64 MPa. However, only the powder obtained *via* the slow-cooling route could be successfully densified. The final dimensions of the pellets are around 8 mm in thickness and 10 mm in diameter. Densities are about 92–93% of the theoretical ones, determined from Rietveld refinement.

X-ray diffraction analysis

The batch synthesis yielded grains of matter measuring several tens of micrometers in size. These grains were not single

crystals and were manually broken with a scalpel, and then selected under a stereomicroscope. They were mounted on microloops, and their diffraction quality was assessed. Single-crystal X-ray diffraction was performed using a Rigaku Synergy S diffractometer equipped with a micro-focus sealed Mo X-ray tube and an Eiger 1M Dectris photon-counting detector. Data reduction was carried out with CrysAlisPro, while structure determination was performed using Jana and Superflip.[54,55]

It is worth noting that, for both quenched and slow-cooled samples, despite the synthesis batches containing some crystals larger than 50 μm, the structure solution by direct or charge-flipping methods only converged for extremely small crystals, less than 10 μm in size. This limitation is due to the high defectiveness of the crystals, as explained in the discussion. Specifically, the crystal used for X-ray diffraction structure determination was found to be fourfold twinned (obverse-reversed and inversion twinning). Even the selected crystal of the slow-cooled sample used for 3D ED, less than 200 nm wide and dominated by the reverse twin variant, included an additional observed twin component corresponding to about 10% in the refinement.

Powder X-ray diffraction (PXRD) data were collected during 24 h at RT using a Bruker D8 Advance Vario 1 two-circle diffractometer (θ–2θ Bragg–Brentano mode) using Cu Kα radiation ($\lambda = 1.5406$ Å) with a Ge (111) monochromator (Johansson type) and a Lynx Eye detector.

The synchrotron PXRD data of the slow cooled sample were collected at room temperature on the end-station CX2 of the MARS (Multi-Analysis On Radioactive Samples) beamline at Synchrotron SOLEIL (Saint-Aubin, France). High-resolution data were acquired in Debye–Scherrer geometry using a set of 24 detectors equipped with a Ge (111) crystal analyzer.[56] The white beam coming from the bending magnet was monochromatized using a Si(220) double-crystal monochromator at 20 keV. Higher harmonics rejection and vertical collimation were achieved using Pt coated mirrors.

XRD data analyses were performed using the Jana2020, FullProf, Faults and WinPlotr software packages.[54,57–59]

TEM sample preparation and characterization

The preparation of TEM lamellae was conducted using a dual-beam focused ion beam system (FIB, Thermoscientific Helios 5 CX). The general procedure is as follows: a small bar-shaped specimen with dimensions of $12 \times 2 \times 5$ μm^3 was extracted from a bulk polycrystalline sample and transferred onto a dedicated copper TEM grid. The operating voltage for this process was 30 kV with a beam current of 9.3 nA. Subsequent thinning of the specimen was performed at 30 kV, during which the beam current was gradually reduced from an initial 0.77 nA down to 80 pA. The thickness of the lamella was controlled within the range of 100–200 nm. Finally, surface cleaning was carried out at low voltage and low beam current conditions (5 kV, 40 pA; 2 kV, 25 pA) to remove the amorphous surface layer, thereby achieving the final thinning of the specimen with the final thickness approximately 50 nm.

TEM characterization, including electron diffraction and atomic-resolution HAADF-STEM imaging, was performed using a double spherical-aberration-corrected electron microscope (Thermoscientific Spectra 300) operated at 300 kV with a beam current of ~50 pA.

Scanning electron micrographs and electron energy dispersive spectroscopy (EDS) images were collected using a JEOL JSM 7200F scanning electron microscope (SEM) equipped with an EDX X-Flash Bruker detector.

3D electron diffraction

3D Electron Diffraction (3D ED)[60] is a technique that uses electron diffraction patterns collected from a single crystal to determine its crystal structure. For this study, precession-assisted 3D ED data were collected using a JEOL F200 transmission electron microscope working at 200 kV, equipped with an ASI Cheetah M3 detector and a Nanomegas Digistar precession unit. Cu_2ZrS_3 pellets were ground in ethanol with an agate mortar, and a drop of the resulting suspension was deposited onto a holey carbon membrane on a Cu mesh grid. 3D ED data were collected at room temperature using the Instamatic program,[61] with a precession angle of 1.25°, and a tilt step of approximately 1° between successive patterns. Data processing was performed with PETS2,[62] and structural refinements were carried out in Jana2020,[63] accounting for both dynamical diffraction effects and electron beam precession. The refined structural parameters of the slow cooled Cu_2ZrS_3 sample are summarized in Table S3. The selected 3D ED dataset was collected over a total rotation range of 113° using a 100 nm beam from a thin crystal edge approximately 140 nm wide, as estimated from bright-field imaging, and 32 nm thick (refined value).

Electrical and thermal property measurement

The electrical resistivity, ρ, and Seebeck coefficient, S, were measured simultaneously using a ULVAC-ZEM3 instrument on bar shaped samples with dimensions $2 \times 3 \times 10$ mm^3 from 300 K up to 700 K, at around 0.1 bar of He. A NETZSCH LFA-457 apparatus was used for measuring the thermal diffusivity under an argon flow. The thermal conductivity, κ, was determined as the product of the volumetric mass, thermal diffusivity, and theoretical heat capacity estimated using the Dulong–Petit approximation. Heat capacity (C_p) measurement have been realized on the Cu_2ZrS_3 sample to confirm the agreement with the experimental Dulong–Petit values. The lattice contribution to the thermal conductivity, κ_L, was determined by considering κ_e as negligible, given the high electronic resistivity (Fig. S1). The value of κ_L is therefore estimated to be equivalent to the total thermal conductivity κ. The estimated measurement uncertainties are 8% for the electrical resistivity and 11% for the thermal conductivity.[64]

Hall effect measurements over the temperature range of 5–300 K were carried out using a Physical Properties Measurement System (PPMS; Quantum Design) under an applied magnetic field of ±9 T.

First-principles calculations

We employ first-principles calculations based on density functional theory (DFT), as implemented in the Vienna *Ab initio*

Simulation Package (VASP).[65–67] Projector augmented wave (PAW) potentials are used to model the interaction between valence electrons and ionic cores. Valence electronic configurations of these elements are S: $3s^2 3p4$, Cu: $3d^{10}4s1$, and Zr: $4s^2 5s^1 4p^6 4d^3$. The exchange–correlation energy functional of electrons is treated within the generalized gradient approximation (GGA) with the Perdew–Burke–Ernzerhof for solids (PBE-sol) parametrization.[68] To capture on-site electronic correlations, we use a Hubbard-U of 4 eV for Cu-3d orbitals. Kohn–Sham (KS) wave functions are represented using a plane wave basis truncated with an energy cutoff of 444 eV. The KS equations are solved iteratively to achieve self-consistent solution such that the total energy per unit cell converges within 10^{-8} eV. Brillouin zone integrations are carried out using uniform k-meshes of $8 \times 8 \times 2$ for $P31c$ and R3 structures. To speed up the convergence of the self-consistent cycles, Gaussian smearing of 0.01 eV is applied to the electronic occupation numbers. Structural optimization is performed until the magnitude of the force on each atom in each direction is less than 1×10^{-3} eV Å^{-1}. In electronic structure calculations, we use the mBJ method to estimate the band gap. Phonon dispersion is obtained from the interatomic force constants determined with the frozen phonon method in a $2 \times 2 \times 1$ supercell, using Phonopy code.[69,70]

Results and discussion

Crystal structure analysis: high potential of Cu_2ZrS_3 for polytypism

The existence of Cu_2ZrS_3 was recently reported for the first time by Li *et al.*[46] The trigonal structure ($P31c$, $a = 6.475$ Å, $c = 12.164$ Å) of this compound consists of an alternate stacking along the c axis of layers of corner-sharing CuS_4 tetrahedra and CdI_2-type layers of edge-sharing ZrS_6 octahedra, with one Cu substituting Zr at every third Zr position, and adopting a distorted CuS_3 trigonal planar geometry.

It was described by the authors as a derivative of the ZrS_2 structure involving the intercalation of Cu between the CdI_2 layers and the substitution of Zr by Cu within the CdI_2 layers. In fact, this structure can be alternatively described as a derivative of the $CuScS_2$ structure ($P3m1$, $a = 3.7333(5)$, $c = 6.098(1)$).[71] Bearing in mind that the $CuScS_2$ structure (Fig. 2a and b) consists of octahedral ScS_2 layers with CdI_2 type configuration (Fig. 2a) stacked with layers of CuS_4 tetrahedra (Fig. 2b), the Cu_2ZrS_3 structure determined by Li *et al.*[46] can be described by the structural formula $Cu[Cu_{1/3}Zr_{2/3}]S_2$. In this way, the Li's Cu_2ZrS_3 structure can be described as being built up of new $[Cu_{1/3}Zr_{2/3}]S_2$ layers (Fig. 2c) derived from the CdI_2 type configuration of "unbalanced $CuZrS_2$" by replacing one octahedral

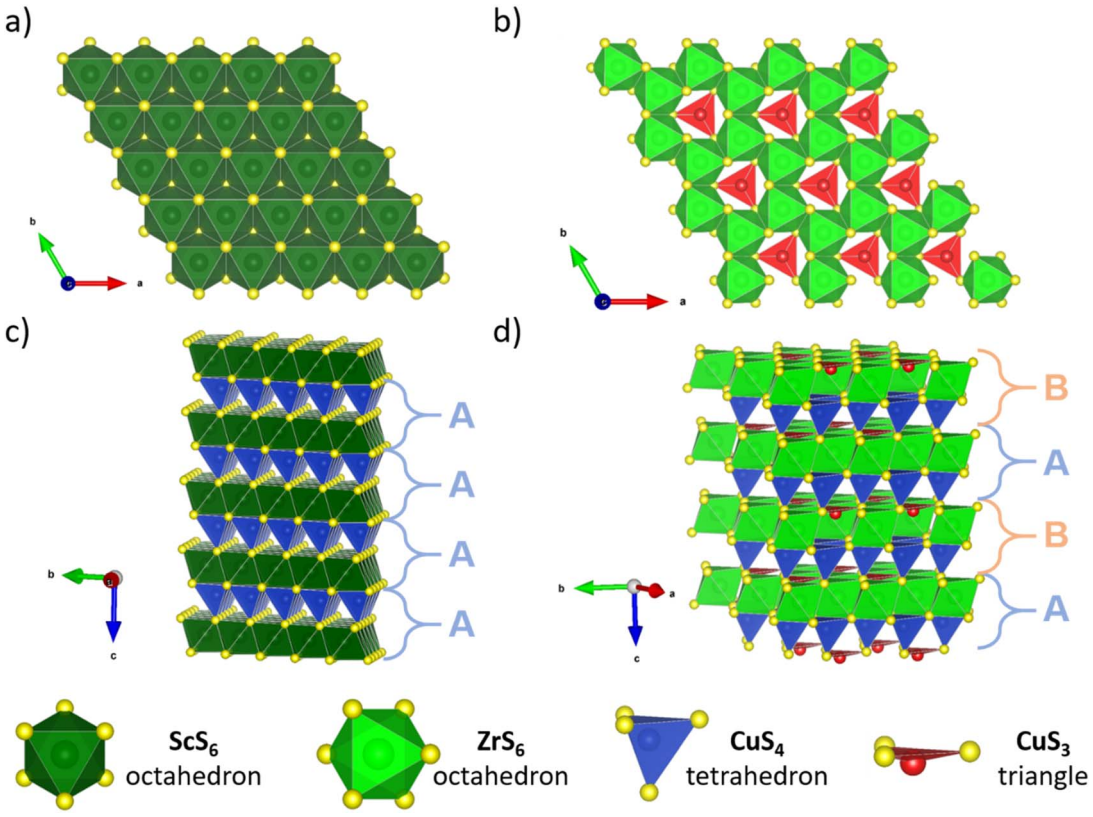

Fig. 2 Structures of $CuScS_2$ (a)–(c) and of Cu_2ZrS_3 as determined by Li *et al.*[46] (b)–(d). The $CuScS_2$ structure is built up of ScS_2 layers (a) of edge-sharing ScS_6 octahedra (dark green coloured) of CdI_2 type layers stacked with (c) layers of corner-sharing CuS_4 tetrahedra (blue coloured). The Cu_2ZrS_3 structure can be described as being derived from $CuScS_2$ by forming $Cu_{1/3}Zr_{2/3}S_2$ layers with the CdI_2 configuration (b) stacked with layers (d) of corner-sharing CuS_4 tetrahedra (blue coloured). Note that in the $Cu_{1/3}Zr_{2/3}S_2$ layers, the CuS_3 triangles (red coloured) correspond to the ordered substitution of Zr by Cu in the edge-sharing ZrS_6 octahedra (green coloured) of the « unbalanced ZrS_2 » layer of the CdI_2-type configuration.

Zr^{4+} out of three by one triangular Cu^{+} in order to maintain the electro-neutrality.

Note that this ordered Cu for Zr substitution corresponds to a displacement of Cu^{+} from the center toward the face of the Zr octahedron allowing a threefold coordination for Cu^{+}. This leads to a new two-dimensional hexagonal lattice with cell transformation $a' = a - b$, $b' = 2b + a$ (see Fig. 3). Both structures, $CuScS_2$ and $Cu[Cu_{1/3}Zr_{2/3}]S_2$, can be described as stacks along the *c*axis of double layers of Cu tetrahedra and Zr (or $CuZr_2$) polyhedra. In the case of $CuScS_2$, these layers (labeled A) exhibit an AA stacking along the *c*axis, leading to a periodicity of 6 Å along this direction (Fig. 2c). In contrast, for $Cu[Cu_{1/3}Zr_{2/3}]S_2$ an ABAB stacking is observed (Fig. 2d), leading to a doubling of the *c* parameter. Such a feature avoids clustering due to substitution along the *c* axis, by introducing a displacement vector in the (*ab*) plane during the stacking of the layers along the *c* axis. In the case of the Cu_2ZrS_3 structure reported by Li *et al.*, the displacement vector is [100] in the $CuScS_2$ cell (blue cell in Fig. 3b) or equivalent (orange arrows in Fig. 3a) with an ABAB stacking.

In summary, the structure reported by Li *et al.* considers an AB stacking arrangement with a vector sequence $[\frac{1}{3}, \frac{2}{3}, 1]$ (thick orange arrows) followed by $[-\frac{1}{3}, -\frac{2}{3}, 1]$ (thick violet arrows), using the substituted $CuScS_2$ layer as a reference. Here, the *c* axis defines the stacking direction of the successive layers (Fig. 3). There exist other equivalent directions for the shifting of the layers (see thin arrows in Fig. 3a), suggesting that this sulfide exhibits a high potential for polytypism. This convention will be used hereafter to describe all other vectors generating new polytypes. Cu_2ZrS_3, as already reported for $CuScS_2$, has a high degree of strain due to the rigid geometric constraint induced by the structure. This strain may explain the limited number of compounds adopting this type of structure, despite its apparent simplicity. Specifically, the coordination of sulfur atoms by metal atoms involves significant distortions to accommodate the substantial difference between Cu–S and Zr–S bond lengths.[71]

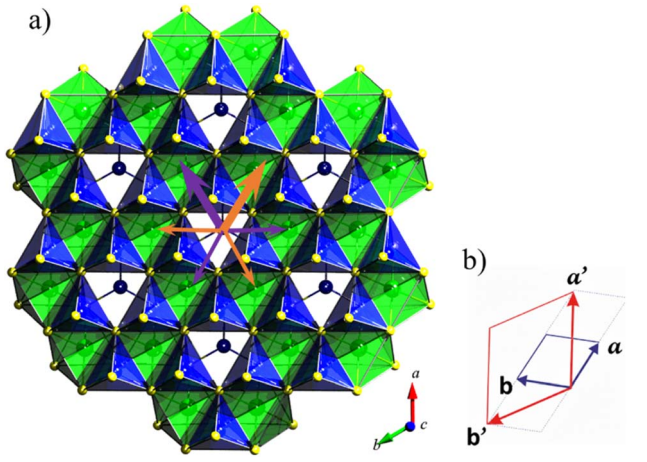

Fig. 3 (a) Representation of Cu_2ZrS_3 considering the substitution of Zr by Cu every three Zr atoms in $CuZrS_2$. The thick orange (or violet) arrows represent the displacement vector necessary in the stacking of Cu_2ZrS_3 in order to avoid the superposition of substitution. The thin arrows represent all equivalent directions by translation. (b) Representation of the relationship between the cells corresponding to Cu_2ZrS_3 and $Cu_{1/3}Zr_{2/3}S_2$ ($CuScS_2$ type) layers, in red and blue, respectively.

Synthesis and structural characterization of two new polytypes and evidence for stacking faults

In order to investigate the impact of different synthesis conditions on the phase composition, two different syntheses were carried out. The first sample was held at 1373 K for 48 hours before being air-quenched (similar to the synthesis conditions reported by Li *et al.* (quenched at 1423 K)), while the second sample underwent slow cooling to RT over 21 hours. Fig. 4a shows the powder X-ray diffraction (PXRD) pattern of our sample quenched from 1373 K, compared with the diffraction pattern calculated from the structure reported by Li *et al.*[46] The two patterns have some similarities but differ in several superstructure peaks, which are in different 2θ positions (inset, Fig. 4a). As those additional reflections cannot be assigned to impurities, it tends to indicate that they probably correspond to the existence of a possible polytypism in this layered compound. Note that polytypism is a special case of polymorphism in which the two-dimensional translations within the layers are essentially preserved but differ only in their stacking sequence. Our hypothesis is supported by the existence of a known polytype, $CuCrSe_2$ ($R3m$, $a = 3.679(1)$, $c = 19.385(5)$),[72] differing from $CuScS_2$ only by the stacking order.

A thorough X-ray diffraction investigation of a single crystal extracted from the air quenched sample (1st tube) was carried out. It allowed us to identify a new polytype of Cu_2ZrS_3 characterized by the $P31c$ space group ($a = 6.47548(16)$ Å, $c = 24.3290(5)$). The agreement factors and atomic parameters are reported in Table S1. The ABCB stacking sequence of the double octahedral/tetrahedral layers of this polytype (Fig. 5d) corresponds to a quadrupling of the *c* parameter of the parent structure $CuScS_2$ (Fig. 5a) and to a doubling of the *c* parameter of the Li's Cu_2ZrS_3 structure that we describe here as a polytype with an AB sequence (Fig. 5b). Coming back to the PXRD patterns, we observe that the calculated PXRD derived from the quenched single-crystal X-ray diffraction (SC XRD) data (green coloured in Fig. 4) shows good agreement with our experimental PXRD pattern. However, both patterns present some discrepancies regarding the relative intensity of some reflections and the existence of broad diffraction peaks in the experimental PXRD pattern, as highlighted by the black arrows in the inset of Fig. 4a. The interpretation of such discrepancy could be supported by a careful examination of SC XRD data and the refined structural model. First, this structure suggests several mixed Zr/Cu occupancy sites (see Table S1) within the octahedral layers, which are unexpected, and even crystallochemically unlikely, considering their respective coordination preferences, namely octahedral for Zr^{4+} and tetrahedral for Cu^{+}. Second, a careful examination of the reciprocal space map reconstruction of the studied crystal reveals diffuse intensity along the *c*-axis, specifically between *hkl* reflections where $h,l \neq 3n$ and $l = 2n + 1$ (Fig. 4b green ovals). These two observations suggest the

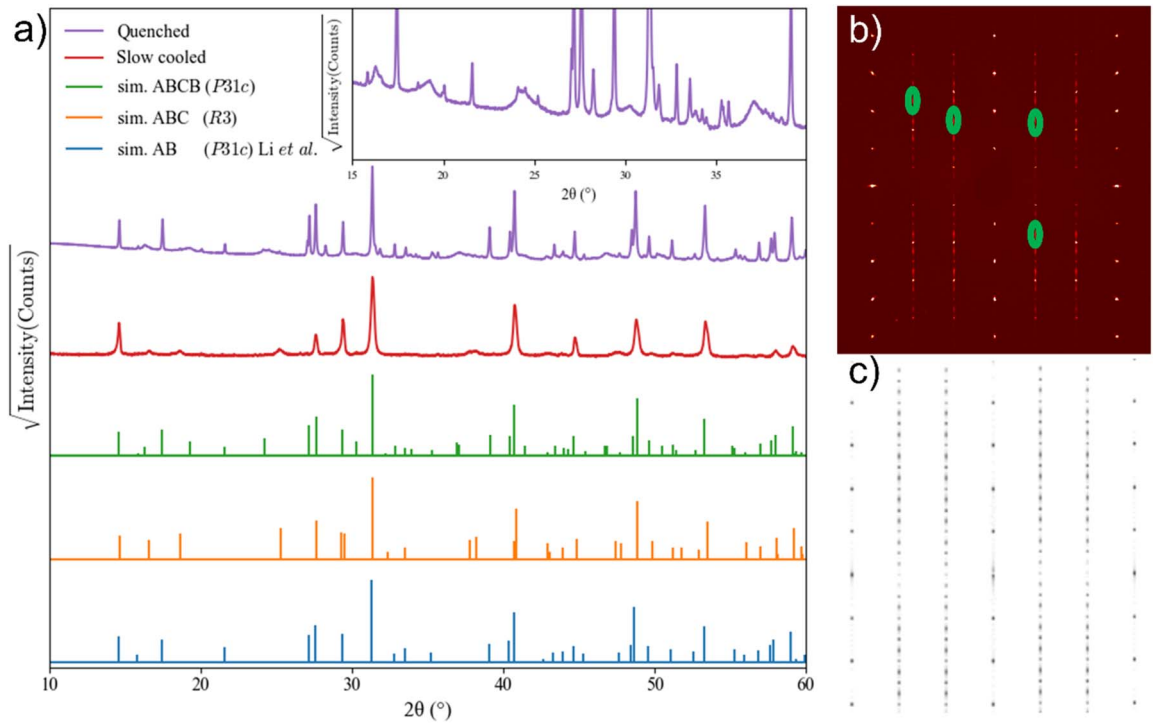

Fig. 4 (a) PXRD pattern of the quenched sample (violet curve), powder diffraction diagram of the slowly cooled sample (red curve), calculated PXRD pattern of the *P31c* structure with ABCB stacking resolved from single crystal data (green curve), calculated PXRD pattern of the *R3* crystal structure with ABC stacking resolved from single crystal data (orange curve) and structure reported by Li *et al.*[46] (blue curve). The inset shows a focus of the experimental PXRD pattern of the quenched sample. Black and red arrows show anomalous broadening and unindexed peaks, respectively. (b) Reciprocal space reconstruction of layer *h0l* for the (a) experimental quenched sample and (c) simulated sample.

presence of stacking faults along the *c*-axis, as the partial occupancy describes a structure with different substitutional order superimposed, while the diffuse scattering describes a partial loss of translational periodicity along the *c* axis. The absence of this feature in common reflections with the $CuScS_2$ type structure strongly indicates that the stacking faults are

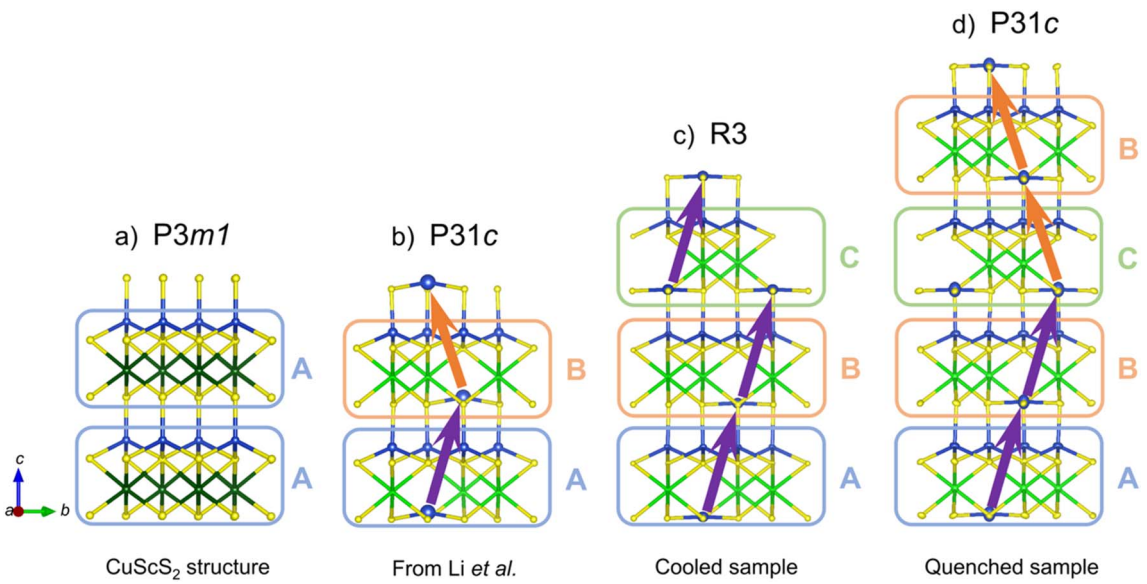

Fig. 5 Comparison of the different polytypes: (a) $CuScS_2$ structure ($a = 3.733$ Å, $c = 6.098$ Å), (b) *P31c* structure reported by Li *et al.*[46] with AB stacking ($a = 6.475$ Å, $c = 12.165$ Å), (c) *R3* structure determined for the quenched sample with ABC stacking ($a = 6.475$ Å, $c = 18.176$ Å) and (d) *P31c* structure determined for the slowly cooled sample with ABCB stacking ($a = 6.475$ Å, $c = 24.329$ Å).

related to the position and ordering of Cu in the CdI_2 layer, while the parent structure remains unaffected. Taking these observations into account, it was possible to simulate the diffraction pattern using the DIFFaX algorithm,[73] considering an intergrowth of the structure reported by Li *et al.*[46] with the structure solved by single crystal, modified to enforce full occupancy at each site. Mathematically, the system was modeled as alternating stacks of two-layer blocks corresponding to the AB and CB stackings discussed previously, with a small probability of missing a layer block. The simulation of the *h0l* reciprocal plane presented in Fig. 4c has been obtained using a 5% probability of stacking error. For the powder diffraction simulation, this probability was increased to 15%. The observed difference between powder and single-crystal diffraction data is likely attributable to the arbitrary selection of single crystals, which typically focuses on less defective specimens.

Although the introduction of stacking faults improved the agreement between the model and the experimental data, as shown in Fig. S2a, the low-intensity sharp peaks (indicated by red arrows in the inset of Fig. 4) remain unaccounted for. Indexing these peaks suggests a trigonal unit cell with lattice parameters $a = 6.47$ Å and $c = 24.33$ Å, which is consistent with a potential polytype that quadruples the c axis of $CuScS_2$, corresponding to a structure composed of four block layers.

Based on those results and with the aim of obtaining a material with fewer stacking faults, we synthesized a new batch of powder by cooling down the sample at 50 K h^{-1} instead of quenching to avoid the formation of stacking faults and to stabilize a crystal structure with three block layers. The structure of this slowly cooled sample was determined using SC XRD, 3D ED and synchrotron PXRD analyses. From SC XRD and 3D ED analyses (Tables S2 and S3, respectively), we found that the crystal structure corresponds to a new polytype ($R3$ space group) characterized by a tripling of the c axis compared to the hypothetical CuS_2 structure. In this polytype, the stacking follows an ABC sequence with stacking vectors [1/3, 2/3, 1] (Fig. 5c). The Rietveld refinement of the synchrotron PXRD pattern, considering this structural model, resulted in excellent agreement between the experimental data and the model, with the presence of stacking faults also being modeled for this slowly cooled sample, as shown in Fig. S2b. In such a case, the stacking sequence has been modelled as an ABC sequence with a 15% probability of passing to a ACB sequence and *vice versa*. It is worth noting that although the probability of a defect is the same as that for the quenched sample, the nature of the defect is different, resulting in a minor perturbation of the lattice. The coordination environments of the atoms have strong similarities to the structure reported by Li *et al.* ($P31c$, AB stacking). Both Zr atoms occupy slightly distorted octahedral sites with an average bond distance to S of 2.65 Å, and the Cu(1) atoms are located in a distorted tetrahedral environment with an average bond distance to S of 2.34 Å. These findings suggest that the atomic layers are only marginally affected by the different stacking arrangements. However, the Cu(2) site shows a notable difference. In both refined structures, obtained from the quenched ($P31c$, ABCB stacking) and cooled ($R3$, ABC stacking) samples, it lies nearly in the plane (0.01 Å) of the trigonal coordination (triangular coordination), whereas, in the structure reported by Li *et al.*, the Cu(2) site is significantly displaced from the plane (0.44 Å). The anisotropic displacement parameters determined by SC XRD data and 3D ED data in Tables S2 and S3 reveal that the Cu atom in triangular coordination exhibits greater displacements compared to the other cations, as observed in Cu_3BiS_3 and even more pronouncedly in the tetrahedrite $Cu_{12}Sb_4S_{13}$.

To verify the crystal structure and assess potential atomic-scale defects, electron diffraction (ED) and high-angle annular dark-field scanning transmission electron microscopy (HAADF-STEM) analyses were carried out on Cu_2ZrS_3 samples subjected to different thermal treatments (Fig. 6). The quenched specimen shows a largely ordered arrangement but also contains dense stacking faults (Fig. 6a and b). High-resolution observations (yellow-framed region) reveal a structure close to that determined by SC XRD, characterized by an ABC-type stacking sequence (*i.e.*, the $R3$ structure). However, local twinning is observed both in HAADF images and SAED patterns (red arrows in Fig. 6a and c), suggesting partial cation disorder. This interpretation is consistent with the corresponding ED patterns, which exhibit diffuse and weakened intensities along the c-axis (white arrows in Fig. 6a and f), features indicative of stacking faults and comparable to those reported in Fig. 4a. The diffuse scattering further confirms the existence of long-range disorder involving copper atoms. Altogether, these observations point toward a local deviation from the ideal $R3$ stacking, ultimately leading to the ABCB-type (*i.e.*, $P31c$ structure) sequence identified by single-crystal refinement. Notably, the ABC-type stacking observed by TEM is not revealed by SC XRD and 3D ED, which reflect the average long-range structure. This apparent discrepancy arises from the coexistence of stacking faults and partial cation disorder, evidenced by single-crystal data and DIFFaX simulations.

In contrast, the slowly cooled sample displays a far more homogeneous and regular structure (Fig. 6d and e). Defects are relatively more abundant in the quenched specimen, whereas in the slowly cooled sample twins are still present but at a much lower density and generally appear as larger well-developed domains, while stacking faults are rarely observed. Elemental mapping (Fig. S3) corroborates this result, revealing a uniform distribution of the constituent elements, with only traces of ZrO_2 detected in a few localized areas (highlighted by a red circle). These findings clearly demonstrate that Cu_2ZrS_3 is highly sensitive under cooling conditions: rapid quenching induces structural disorder and stacking faults, whereas controlled slow cooling favors stacking reorganization and yields a thermodynamically stable crystalline phase.

DFT calculations

The calculated formation energies of the three polytypes, described in Fig. 5, are comparable within the margin of error (Table S4), which is consistent with the experimental finding that the atomic layers are only marginally affected by the different stacking arrangements. Optimized lattice parameters for both ABCB and ABC polytypes are consistent with the

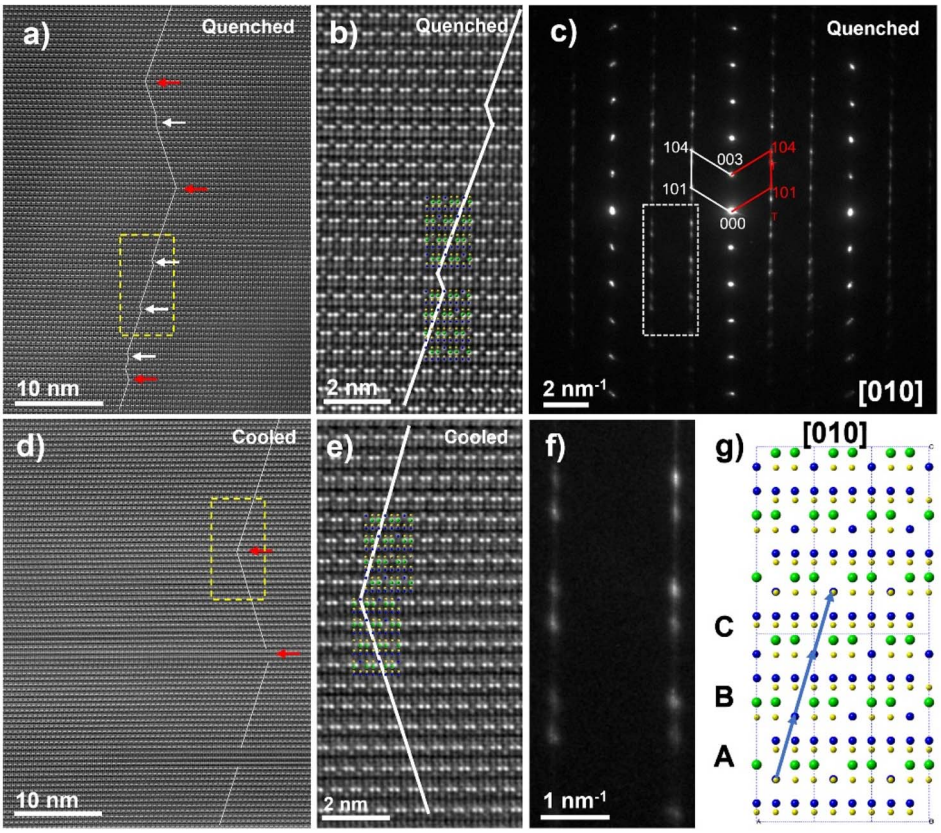

Fig. 6 TEM characterization of the Cu_2ZrS_3 samples: quenched (a)–(c) and (f), slowly cooled (d) and (e), and atomic structure viewed along the [010] crystallographic orientation (g). The regions marked with yellow dotted lines in (a) and (d) correspond to images (b) and (e), respectively. The selected electron diffraction pattern of the quenched sample is shown in (c), with the highlighted region shown in (f). In HAADF images, the white lines are guided for the stacking sequences, and the white and red arrows indicate the stacking faults and twin boundaries, respectively.

experimental data, summarized in Table 1. Error in lattice parameters is negative, which is attributed to the use of PBEsol.

To understand the properties of Cu_2ZrS_3, we examine the electronic structure and orbital projected density of states (pDOS) of the two structures (with ABC and ABCB stacking). Valence band maxima (VBM) and conduction band minima (CBM) for the ABC stacked structure are at Γ and T (0.5, 0.5, 0.5), respectively, while that for ABCB stacked structure are located at Γ and M (0.5, 0, 0), respectively, with an indirect bandgap of 0.99 eV in both the structures. The electronic states near the conduction band minimum (CBM) are dominated by Zr-d states, while that for the valence band maximum (VBM) are arising from Cu-d orbitals (Fig. 7). Visualizations of wavefunctions at the VBM and CBM show that the VBM is composed of S-p and the CBM comprises (i) wavefunctions which that overlap between Zr–Zr and Zr–S and (ii) Zr-d (Fig. S4c–f).

Table 1 Lattice parameters of the Cu_2ZrS_3 structure with ABC and ABCB stackings. Comparison between experimental and optimized values along with percentage error

	ABCB			ABC		
Parameter	Expt.	Opt.	% Error	Expt.	Opt.	% Error
a (Å)	6.47	6.38	−1.39	6.47	6.38	−1.39
b (Å)	6.47	6.38	−1.39	6.47	6.38	−1.39
c (Å)	24.32	23.83	−2.01	18.24	17.88	−1.97

To study the stability of these structures, we determine their phonon dispersion using conventional unit cells. The systems do not exhibit any imaginary frequencies in the Brillouin zone, which confirms their dynamical stability. The highest frequency mode is at $\omega = 382$ cm^{-1} for the ABC stacked structure and at 354 cm^{-1} for the ABCB stacked structure (Fig. 7b and f). There are four gapped regions in the phonon dispersion of the ABC stacked structure: 0–150 cm^{-1}, 150–200 cm^{-1}, 200–280 cm^{-1} and greater than 280 cm^{-1}. However, in ABCB stacking, there is mixing and merging of 200–280 cm^{-1} and greater than 280 cm^{-1} regions. The ionic motion projected phonon DOS (phDOS) reveals that S dominates at frequencies above 200 cm^{-1}, whereas the low-frequency modes are mainly contributed by Cu and Zr, with an overall higher phDOS intensity observed for ABCB stacking compared to the ABC one (Fig. 7c and g). Additionally, a distinct peak corresponding to Cu appears near 280 cm^{-1} in the case of ABC, which is absent in the ABCB stacked structure. Since Cu atoms in Cu_2ZrS_3 occur in distinct three-fold (S_3) and four-fold (S_4) coordination environments, the projection has been resolved for the two Cu

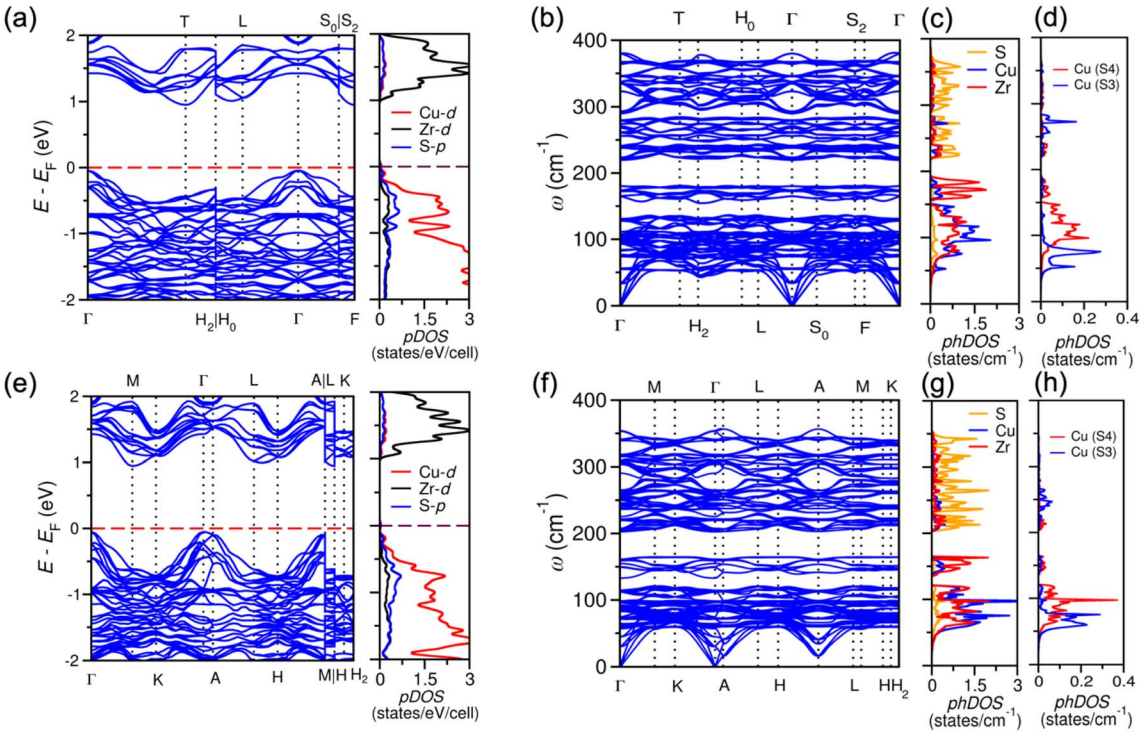

Fig. 7 Electronic structures and orbital projected density of states (pDOS) of (a) ABC and (e) ABCB stacked structures. An indirect bandgap of 0.99 eV is present in both cases. The CB is dominated by Zr-d and the VB comprises Cu-d. Phonon dispersion and density of states (phDOS) of Cu_2ZrS_3 in structures with ((b) and (c)) ABC and ((f) and (g)) ABCB stacking confirm their dynamical stability. The phDOS of Cu projected onto three and four fold coordinations ((d) and (h)) shows dominant contribution of S_3 coordinated Cu at frequencies below 80 cm^{-1}.

coordinations, revealing that Cu in three-fold coordination contributes more significantly to modes below $\omega = 80$ cm^{-1} (Fig. 7d and h). In the frequency range of 100–230 cm^{-1}, the phonon modes are dominantly contributed by four-fold coordinated Cu atoms while above this frequency, the contribution from three-fold coordinated Cu atoms increases once again.

Vibrational properties

To understand the optical phonon characteristics of the *P*31*c* and *R*3 space groups in Cu_2ZrS_3, Raman spectroscopy was performed across a temperature range of 77–343 K, focusing on the spectral range 53–500 cm^{-1}. At room temperature (300 K), the Raman spectrum for the *R*3 phase displays eight modes: three are found in the low-frequency region below 150 cm^{-1} and five are located between 150 and 500 cm^{-1}. In contrast, for the *P*31*c* phase, only seven modes are observed at room temperature, with three in the low-frequency region and four in the high-frequency region (Fig. S5). The symmetry analysis of the ABC stacked structure (*R*3 space group) indicates that the Raman-active phonon modes correspond to the irreducible representations *A* and *E* (E_1 and E_2). In contrast, for the ABCB stacked structure (*P*31*c* space group), the Raman-active modes correspond to A_1 and *E* representations. We visualized the Raman-active modes of ABC and ABCB polytypes (shown in Fig. S6 and S7, respectively) to find their mutual correspondence. Assignment of irreducible representations to modes of ABC and ABCB stacked structures are listed in Table 2, respectively.

Vibrational modes at 89 and 120 cm^{-1} of the ABC stacked structure are comparable to those in the ABCB stacked structure, appearing at 94 and 116 cm^{-1}, respectively. Despite the comparable frequencies, their Raman intensities are higher in the ABC structure. Zr displacements dominate the lower frequency mode of the ABC stacked structure (Fig. S6), while displacement of Cu in the four-fold coordination dominates in the ABCB stacked structure (Fig. S7). In the higher-frequency vibration, both structures involve the same atomic species, but the ABC stacked structure shows larger eigen-displacements oriented along the S–Cu bond, leading to its enhanced Raman activity and hence stronger intensity. Another noteworthy

Table 2 Comparison of the measured and calculated frequencies of Raman modes for *R*3 and *P*31*c* phases

*R*3			*P*31*c*		
Exp. (cm^{-1})	Estimated (cm^{-1})	Irrep.	Exp. (cm^{-1})	Estimated (cm^{-1})	Irrep.
65	56	*A*	65	64	A_1
89	83	*A*	94	91	A_1
120	129	*E*	116	114	*E*
166	172	*E*	174	161	*E*
231	240	*A*	241	241	A_1
256	262	*A*	330	339	A_1
334	334	*E*	371	354	A_1
374	367	*A*			

feature is the presence of two A modes at 231 and 256 cm^{-1} in the ABC stacked structure, whereas a single mode is observed at 241 cm^{-1} in the ABCB stacked structure.

Temperature dependent Raman spectra of Cu_2ZrS_3 (Fig. 8a) exhibit a red shift of peaks towards lower frequencies, providing a clear picture of phonon softening with increasing temperature. This behavior is typically associated with anharmonic lattice interactions and thermal expansion effects. We have estimated the phonon lifetime, a key parameter that characterizes phonon propagation and scattering behavior within a material, by applying the energy–time uncertainty relation, $\frac{\Gamma}{\hbar} = \frac{1}{\tau}$,[74–76] where τ is the phonon lifetime, Γ is the FWHM of Raman modes in cm^{-1}, and $\hbar = \frac{h}{2\pi} = 5.3 \times 10^{-12}$ cm^{-1} s^{-1}.

The corresponding FWHM values shown in Fig. 8b and the calculated phonon lifetimes (τ) for the Raman-active modes at 65, 166, and 374 cm^{-1} are presented in Fig. 8c. As clearly observed, the phonon lifetimes of the optical modes decrease progressively with increasing temperature. This reduction in phonon lifetime reflects the increase in the lattice vibrations and points to strong phonon scattering processes, which play a crucial role in limiting lattice thermal conductivity.

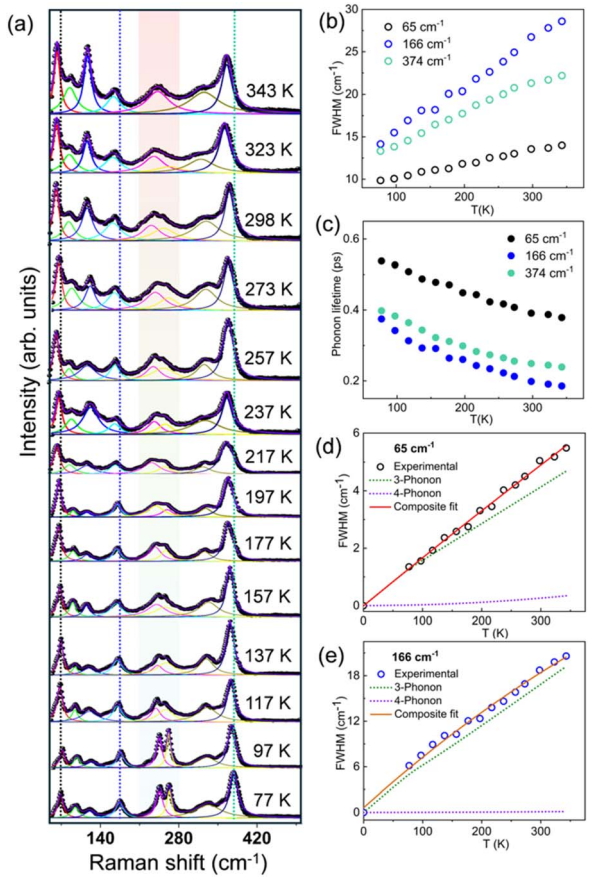

Fig. 8 (a) Temperature-dependent Raman spectra of Cu_2ZrS_3 measured from 77 to 343 K. (b) Full width at half maximum (FWHM) of the Raman modes at 65, 166, and 374 cm^{-1} as a function of temperature. (c) Calculated phonon lifetimes corresponding to the 65, 166, and 374 cm^{-1} Raman modes. (d) and (e) Decomposition of the FWHM of the 65 cm^{-1} and the 166 cm^{-1} Raman modes into anharmonic contributions from three-phonon and four-phonon scattering processes in Cu_2ZrS_3.

To calculate phonon anharmonicity we fitted the FWHM using the Klemens model, as described by the equation below.[77,78]

$$\Gamma(T) = \Gamma_0 + A\left(1 + \frac{2}{\{e^x - 1\}}\right) + B\left(1 + \frac{3}{\{e^y - 1\}} + \frac{3}{\{e^y - 1\}^2}\right)$$

The variables x and y are expressed as: $x = \frac{hc\omega_0}{2K_BT}$ and $y = \frac{hc\omega_0}{3K_BT}$, where ω_0 represents the intrinsic frequency of the optical phonon mode and Γ_0 denotes the peak broadening attributed to disorder and scattering. A and B are fitting parameters corresponding to three-phonon and four-phonon anharmonic interactions, respectively.

The anharmonic contributions for the low-frequency 65 cm^{-1} and 166 cm^{-1} modes are shown in Fig. 8d and e, respectively, and the extracted values of the fitting parameters (A and B) are listed in Table S5. The significantly larger three-phonon parameter (A) than the four-phonon parameter (B) clearly indicates that three-phonon scattering is the dominant anharmonic decay mechanism in Cu_2ZrS_3. Furthermore, we conducted temperature-dependent Raman spectroscopy (133–348 K) on the ABCB stacked structure to explore the temperature-induced changes in the optical phonon modes. A thorough analysis, akin to that performed for the $R3$ space group, employed the Klemens model for the phonon mode at 65 cm^{-1}, as depicted in Fig. S8. The results reveal that similar to the ABC-stacked structure ($R3$ space group), the anharmonicity in the ABCB-stacked structure ($P31c$ space group) for this mode is predominantly governed by three-phonon scattering processes, which correlate with a pronounced reduction in phonon lifetimes as the temperature increases. The prominence of three-phonon processes, especially in low-frequency modes, indicates effective phonon scattering pathways that play a role in decreasing the lattice thermal conductivity (κ_L) in Cu_2ZrS_3.

Thermal properties

The total thermal conductivity (κ) of the slowly cooled sample was measured in the direction perpendicular to the pressing axis during sintering over a wide temperature range from 5 to 673 K, as shown in Fig. 9a. No thermal conductivity measurements were performed on the quenched sample. As explained in the experimental section, it was not possible to obtain a sufficiently dense bulk sample free of oxides, which is suitable for reliable measurements. Note that XRD analyses, performed on the slowly cooled sample before and after LFA measurement, evidenced that no notable structural changes occur during

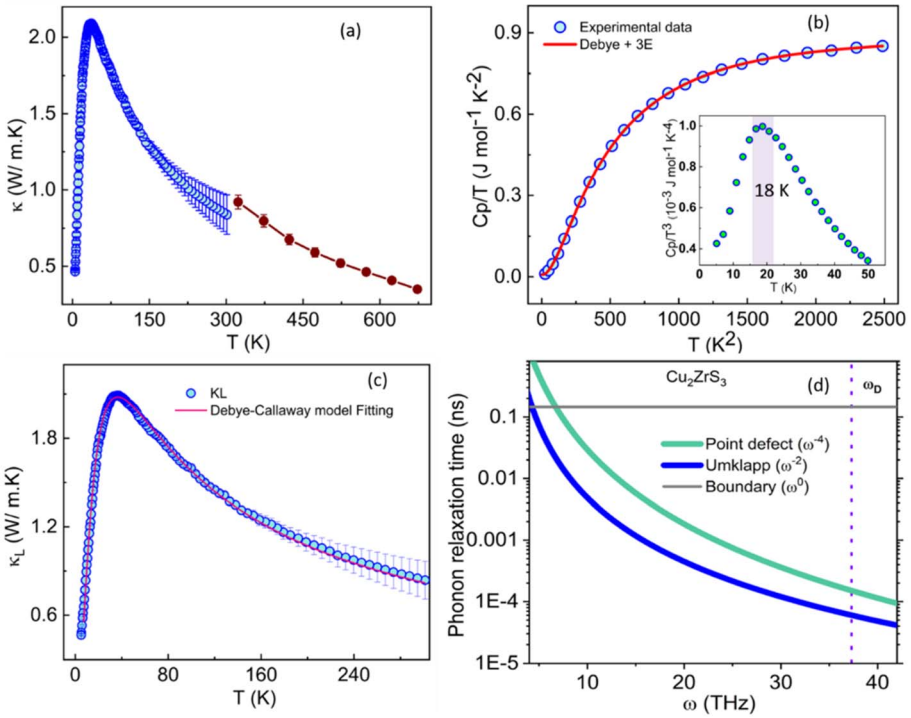

Fig. 9 The temperature-dependent total thermal conductivity (κ) of the slowly cooled Cu_2ZrS_3 sample measured using PPMS (5–300 K) and LFA (300–673 K). (b) Low temperature C_p/T *versus* T^2 plot of Cu_2ZrS_3 fit with the Debye–Einstein model. The inset illustrates the presence of a pronounced peak in the C_p/T^3 *vs.* T plot. (c) The lattice thermal conductivity data for Cu_2ZrS_3 are presented, with the red solid line representing the fit to the data using the Debye–Callaway model. (d) The calculated phonon relaxation time for different scattering mechanisms involved in lattice thermal conductivity is depicted as a function of frequency, where ω_D denotes the Debye frequency.

measurement, as shown in the Fig. S9. This confirms that the *R*3 phase remains stable through the processing and measurement steps. Furthermore, a thermal cycling test was performed during the thermal conductivity measurements, covering the temperature range up to 700 K under a controlled atmosphere. The observed hysteresis in the data is minimal, further supporting the thermal stability of the *R*3 phase under the studied conditions. The electrical resistivity and Seebeck coefficient data were only successfully measured below room temperature (Fig. S10). Indeed, it was not possible to perform electrical transport measurements above room temperature. The phase instability is most probably related to ionic migration and sensitivity of Zr to oxidation. Further investigations are necessary to clarify these instability issues.

In the low-temperature regime, the electronic and lattice contributions were calculated using the Wiedemann–Franz law, $\kappa_e = \frac{LT}{\rho}$, where L is the Lorenz number, was applied. The model of the single parabolic band[79] is utilized to consider the temperature dependence of the Lorenz number. At low temperatures, κ_L initially increases with increasing temperature, reaching a well-defined peak at 38 K, where it attains a maximum value of 2.08 W m^{-1} K^{-1}. Beyond this point, κ_L begins to decline due to the growing influence of phonon–phonon Umklapp scattering, which restricts thermal transport in crystalline solids. With increasing temperature, the lattice thermal conductivity (κ_L) decreases progressively from 0.83 W m^{-1} K^{-1} at room temperature to 0.34 W m^{-1} K^{-1} at 673 K, reflecting the growing influence of phonon–phonon Umklapp scattering, which increasingly limits thermal transport in crystalline solids.

To elucidate the origin of the experimentally observed low lattice thermal conductivity (κ_L) in the slowly cooled Cu_2ZrS_3 sample, we have measured the low-temperature heat capacity in the range of 5–49 K, as shown in Fig. S11. The C_p data were analyzed using the Debye–Einstein model, as the single Debye model alone was insufficient to accurately capture the experimental behavior. The C_P/T *versus* T^2 plot shows good agreement with the fitted model, as shown in Fig. 9b. The following equation was used to model the data within the Debye–Einstein framework:[80]w

$$\frac{C_P}{T} = \gamma + \beta T^2 + \sum_n \left((A_n)(\theta_{E_n})^2 \times \left(T^2\right)^{-\frac{3}{2}} \times \frac{e^{\theta_{E_n}/T}}{\left(e^{\theta_{E_n}/T} - 1\right)^2} \right)$$

here the first term in the equation, γ known as the Somerfield constant, denotes the electronic contribution. The next term, β relates to the lattice contribution and is expressed as, $\beta = C(12\pi^4 N_A K_B/5) \times (\theta_D)^{-3}$, where N_A denotes Avogadro's number, k_B is the Boltzmann constant, and θ_D represents the Debye temperature. The parameter C is defined by the equation $C = 1 - \sum_n A_n/3NR$, where N indicates the number of atoms per formula unit, and R is the universal gas constant. The third term

in the equation accounts for the influence of Einstein oscillators, with A_n acting as the prefactor and θ_{E_n} denoting the Einstein temperature associated with the nth oscillator mode. The analysis of the fitted C_p data reveals three distinct Einstein temperatures, 50.83 K (35.27 cm^{-1}), 95.68 K (66.38 cm^{-1}), and 156.47 K (108.56 cm^{-1}). These characteristic energies correspond well with the phonon features identified in the dispersion curves, namely the flat phonon branches at ~107 and ~56 cm^{-1}, associated with local vibrations of 4- and 3-fold-coordinated Cu ions, and the weakly dispersed parabolic modes near 34 cm^{-1} at the Γ point, involving coupled Zr–Cu motions. The former reflects localized structural disorder of Cu ions, while the latter corresponds to out-of-phase collective oscillations of adjacent layers, together accounting for the low-frequency vibrational modes captured in the heat-capacity fit. Additionally, the Debye temperature (θ_D) for Cu_2ZrS_3 was found to be 285 K. The fitting parameters are given in SI Table S6. Based on the calculation from phonon DOS, the Cu and, to some extent, Zr atoms contribute to the low energy optical phonon modes. The inset of Fig. 9b illustrates the non-Debye behavior from the C_p/T^3 *vs.* T plot. In Cu_2ZrS_3, a distinct boson peak is present at 18 K. The presence of the boson peak at low temperatures indicates a strong coupling between heat-carrying acoustic modes and low-energy localized optical phonons, thereby contributing to a reduction in lattice thermal conductivity (κ_L) to a value of 0.34 W m^{-1} K^{-1} at 673 K.

Determining sound velocity is very important for grasping the energy dynamics of heat-transmitting acoustic phonon modes.[81] For Cu_2ZrS_3 in the $R3$ polytype, the experimentally measured longitudinal (V_L) and transverse sound velocities (V_T) are 3206 m s^{-1} and 1769 m s^{-1}, respectively, resulting in an average velocity (V_S) of 1971 m s^{-1} (eqn S(1)). The relatively low sound velocity, in comparison to the Cu_2S system,[82] indicates weak phonon transport, which significantly contributes to the inherently low lattice thermal conductivity. In addition, the Grüneisen parameter of 1.660 further reflects anharmonicity within the lattice, which promotes phonon–phonon scattering and thus reinforces the suppression of thermal transport.

In order to understand the distinct scattering mechanisms that influence lattice thermal conductivity (κ_L), the Debye–Callaway model was used to interpret our experimental data (Fig. 9c). The Debye–Callaway model is given as:[83]

$$\kappa_L = \frac{k_B}{2\pi^2 V_s}\left(\frac{k_B T}{\hbar}\right)^3 \int_0^{\frac{\theta_D}{T}} \frac{x^4 e^x}{\tau_{ph}^{-1}(x)(e^x-1)^2}\,dx$$

In the above equation k_B signifies the Boltzmann constant, $\hbar$ denotes the reduced Planck constant and $x = \frac{\hbar\omega}{k_B T}$ is a dimensionless frequency variable that simplifies the Debye integration. The term τ_{ph} represents the phonon relaxation time, which is linked to phonon scattering. According to Matthiessen's rule, the scattering rate is mathematically defined as, $\tau_{ph}^{-1} = \tau_B^{-1} + \tau_D^{-1} + \tau_U^{-1}$, where τ_B^{-1} represents boundary scattering $\left(\tau_B^{-1} = \frac{vs}{L}\right)$, τ_D^{-1} signifies point defect scattering $(\tau_D^{-1} = A\omega^4)$, and τ_U^{-1} pertains to Umklapp scattering $\left(\tau_U^{-1} = B\omega^2 T e^{\frac{-\theta_D}{mT}}\right)$. Including boundary scattering in the model is essential for accurately representing thermal conductivity at low temperatures, while other scattering processes are significant at moderate to high temperatures.[84–87] Here, V_s denotes the sound velocity, θ_D represents the Debye temperature, L signifies the grain size, m is a dimensional constant, and A and B are fitting parameters, as detailed in Table S7. Fig. 9d depicts the phonon relaxation times as a function of phonon frequency for the three main scattering mechanisms in Cu_2ZrS_3. The trend indicates that the intrinsic Umklapp scattering has a shorter phonon relaxation time and it dominates over point defect scattering. Stacking faults in Cu_2ZrS_3 may also suppress thermal conductivity by breaking phonon propagation paths. They introduce local lattice distortions and act as phonon scattering centres for long wavelengths phonons. This disorder, together with the intrinsically soft lattice and low-lying phonon modes, enhances anharmonic interactions and shortens phonon lifetimes, leading to the observed low κ_L. However, as no dense and phase-pure bulk sample of the quenched material was successfully synthesized, these interpretations remain speculative and lack direct experimental confirmation.

Conclusion

This comprehensive study demonstrates that two new polytypes of Cu_2ZrS_3 can be stabilized by carefully tuning the synthesis conditions. Analyses combining powder and SC XRD/3D ED diffraction with high-resolution TEM reveal that the structure cannot be captured by a single crystallographic model. Instead, the compound exhibits a strong tendency toward polytypism and stacking faults. In particular, multiple structural variants coexist, most notably the $P31c$ (ABCB) and $R3$ (ABC) polytypes, in addition to the previously reported $P31c$ (AB) form reported by Li *et al.* These polytypes share very similar local arrangements but differ in their stacking sequences. Theoretical modeling also confirms the stability of the two experimentally observed polytypes and provides insight into their electronic and vibrational properties. Both exhibit an indirect band gap of ~1 eV, with conduction bands dominated by Zr d orbitals and valence bands by Cu d orbitals. Despite their close energetic proximity, subtle differences in the electronic structure and phonon dispersion between the two stacking variants point to possible variations in carrier mobility and thermal transport efficiency. These distinctions highlight the decisive impact of the stacking sequence on the macroscopic properties of Cu_2ZrS_3, even though the local structural motifs remain nearly identical.

Regarding transport properties, the polycrystalline Cu_2ZrS_3 ($R3$ polytype) bulk compound displays an ultralow lattice thermal conductivity of 0.35 W m^{-1} K^{-1} at 673 K, ranking among the lowest ever reported for metal sulfides. The threefold coordination of copper promotes anisotropic vibrations that couple with low-energy optical phonon modes, thereby driving the emergence of such exceptionally low thermal conductivity.

Both DFT calculations and Raman spectroscopy measurements highlight the crucial role of triangularly coordinated Cu cations in phonon scattering.

The findings reported here open several promising directions for future work. First, the pronounced tendency of Cu_2ZrS_3 toward polytypism and stacking disorder suggest that synthetic control over stacking sequences could be leveraged as a powerful strategy to tune both electrical and thermal transport properties. Exploring how synthesis parameters (temperature profiles, cooling rates, or chemical environment) govern the relative stability and distribution of polytypes could lead to tailored structures and microstructures with optimized thermoelectric properties. Second, the exceptionally low lattice thermal conductivity identified in the *R*3 polytype highlights the potential of Cu_2ZrS_3 as a potential thermoelectric material. Future studies should investigate carrier doping and defect engineering to adjust electrical conductivity and the Seebeck coefficient, thereby unlocking the full potential of this compound for energy conversion applications. Third, the similarities with other Cu-rich systems such as tetrahedrite $Cu_{12}Sb_4S_{13}$ and Cu_3BiS_3 confirm that triangularly coordinated copper environments represent a more general design principle for achieving ultralow thermal conductivity in sulfides. Extending this concept to related sulfide compounds or to mixed-anion frameworks could provide a broader family of low-thermal-conductivity materials.

Author contributions

Lucas Le Gars (conceptualization: equal; formal analysis: lead; investigation: lead; supervision: equal; writing – original draft: lead; writing – review & editing: equal). Sakshi Verma (formal analysis: equal; writing – original draft: supporting; writing – review & editing: supporting). Minati Tiadi (formal analysis: equal; writing – original draft: supporting; writing – review & editing: supporting). Carmelo Prestipino (conceptualization: equal; formal analysis: equal; supervision: equal; writing – original draft: equal; writing – review & editing: equal). Animesh Das (formal analysis: equal; writing – review & editing: supporting). Bin Zhang (formal analysis: equal; writing – original draft: supporting; writing – review & editing: supporting). Olivier Perez (formal analysis: equal; writing – review & editing: supporting). Philippe Boullay (formal analysis: equal; writing – review & editing: supporting). Denis Menut (formal analysis). Bernard Raveau (conceptualization: supporting; writing – original draft: supporting; writing – review & editing: supporting). Gaëlle Riou (formal analysis: supporting; writing – review & editing: supporting). Adèle Renaud (formal analysis: equal; writing – review & editing: supporting). Kanishka Biswas (formal analysis: equal; writing – review & editing: supporting). Umesh V. Waghmare (formal analysis: equal; writing – review & editing: supporting). Xiaoyuan Zhou (writing – review & editing: supporting). Koichiro Suekuni (formal analysis: equal; writing – original draft: supporting; writing – review & editing: supporting). Emmanuel Guilmeau (conceptualization: lead; formal analysis: equal; supervision: equal; writing – review & editing: equal).

Conflicts of interest

There are no conflicts to declare.

Data availability

The data supporting this article have been included as part of the supplementary information (SI). Supplementary information: measurement of the resistivity of Cu_2ZrS_3 at low temperature, Rietveld refinement of synchrotron XRD patterns of the quenched sample and the slow cooled sample, EDX mapping of the slow-cooled Cu_2ZrS_3 sample, crystal structures and visualization of wavefunctions at band edges of Cu_2ZrS_3, optimized structures obtained with ABC and ABCB stacking of its layers, visualization of wavefunctions at the VBM shows S-p orbitals for ABC and ABCB stackings, room temperature Raman spectra of Cu_2ZrS_3 in the *R*3 space group, visualization of the Raman active modes of the *R*3 phase, visualization of the Raman active modes of the *P*31*c* phase, temperature-dependent Raman spectra of the *P*31*c* Cu_2ZrS_3 compound measured from 133 to 348 K, full width at half maximum of the Raman modes as a function of temperature, calculated phonon lifetimes, decomposition of the FWHM of the 65 cm^{-1} Raman mode, temperature dependence of the thermal conductivity of the slow-cooled sample, XRD pattern of the samples before and after LFA measurement, temperature-dependence of the electrical conductivity and the Seebeck coefficient of the Cu_2ZrS_3 sample, low temperature heat capacity of Cu_2ZrS_3, structural resolution from single crystal of the quenched sample, structural resolution from X-ray single crystal of the slow cooled sample, structural resolution from dynamic refinement of single crystal of the slow cooled sample, calculated formation energies of Cu_2ZrS_3 for different stacking sequences, calculated fitting parameters from the Klemens model for Cu_2ZrS_3, parameters obtained from the fitting of low-temperature C_p/T *vs.* T^2 data of Cu_2ZrS_3 using the Debye–Einstein model with three Einstein oscillators, and the Debye–Callaway model fitted parameter of Cu_2ZrS_3 in the R3 polytype. See DOI: https://doi.org/10.1039/d5ta10102f.

Acknowledgements

L. L. G., E. G. and K. S. thank the JSPS for the fellowship granted through the JSPS Summer Program 2023 (ID: SP23209). E. G. and M. T. thank the Normandy Region for financial support. SV acknowledges JNCASR for a research fellowship. UVW acknowledges support from a JC Bose grant (2025-0210) of ANRF India. K. B. acknowledges financial support from the Swarnajayanti fellowship grant (SB/SJF/2019-20/06), Core Research Grant (CRG/2023/826), and Anusandhan National Research Foundation (ANRF), DST.

References

1 H. Kim, G. Park, S. Park and W. Kim, Strategies for Manipulating Phonon Transport in Solids, *ACS Nano*, 2021, **15**(2), 2182–2196, DOI: 10.1021/acsnano.0c10411.

2 X. Qian, J. Zhou and G. Chen, Phonon-Engineered Extreme Thermal Conductivity Materials, *Nat. Mater.*, 2021, **20**(9), 1188–1202, DOI: 10.1038/s41563-021-00918-3.
3 T. Ghosh, M. Dutta, D. Sarkar and K. Biswas, Insights into Low Thermal Conductivity in Inorganic Materials for Thermoelectrics, *J. Am. Chem. Soc.*, 2022, **144**(23), 10099–10118, DOI: 10.1021/jacs.2c02017.
4 J. He, Y. Xia, W. Lin, K. Pal, Y. Zhu, M. G. Kanatzidis and C. Wolverton, Accelerated Discovery and Design of Ultralow Lattice Thermal Conductivity Materials Using Chemical Bonding Principles, *Adv. Funct. Mater.*, 2022, **32**(14), 2108532, DOI: 10.1002/adfm.202108532.
5 C. Dames, Ultrahigh Thermal Conductivity Confirmed in Boron Arsenide, *Science*, 2018, **361**(6402), 549–550, DOI: 10.1126/science.aau4793.
6 N. P. Padture, M. Gell and E. H. Jordan, Thermal Barrier Coatings for Gas-Turbine Engine Applications, *Science*, 2002, **296**(5566), 280–284, DOI: 10.1126/science.1068609.
7 J. Yang, X. Wen, H. Xia, R. Sheng, Q. Ma, J. Kim, P. Tapping, T. Harada, T. W. Kee, F. Huang, Y.-B. Cheng, M. Green, A. Ho-Baillie, S. Huang, S. Shrestha, R. Patterson and G. Conibeer, Acoustic-Optical Phonon up-Conversion and Hot-Phonon Bottleneck in Lead-Halide Perovskites, *Nat. Commun.*, 2017, **8**(1), 14120, DOI: 10.1038/ncomms14120.
8 X.-L. Shi, J. Zou and Z.-G. Chen, Advanced Thermoelectric Design: From Materials and Structures to Devices, *Chem. Rev.*, 2020, **120**(15), 7399–7515, DOI: 10.1021/acs.chemrev.0c00026.
9 G. J. Snyder and E. S. Toberer, Complex Thermoelectric Materials, *Nat. Mater.*, 2008, **7**(2), 105–114, DOI: 10.1038/nmat2090.
10 X. Shi, J. Yang, J. R. Salvador, M. Chi, J. Y. Cho, H. Wang, S. Bai, J. Yang, W. Zhang and L. Chen, Multiple-Filled Skutterudites: High Thermoelectric Figure of Merit through Separately Optimizing Electrical and Thermal Transports, *J. Am. Chem. Soc.*, 2011, **133**(20), 7837–7846, DOI: 10.1021/ja111199y.
11 B. C. Sales, D. Mandrus and R. K. Williams, Filled Skutterudite Antimonides: A New Class of Thermoelectric Materials, *Science*, 1996, **272**(5266), 1325–1328, DOI: 10.1126/science.272.5266.1325.
12 T. Takabatake, K. Suekuni, T. Nakayama and E. Kaneshita, Phonon-Glass Electron-Crystal Thermoelectric Clathrates: Experiments and Theory, *Rev. Mod. Phys.*, 2014, **86**(2), 669–716, DOI: 10.1103/RevModPhys.86.669.
13 G. S. Nolas, J. L. Cohn, G. A. Slack and S. B. Schujman, Semiconducting Ge Clathrates: Promising Candidates for Thermoelectric Applications, *Appl. Phys. Lett.*, 1998, **73**(2), 178–180, DOI: 10.1063/1.121747.
14 A. Bhui, M. Dutta, M. Mukherjee, K. S. Rana, A. K. Singh, A. Soni and K. Biswas, Ultralow Thermal Conductivity in Earth-Abundant $Cu_{1.6}Bi_{4.8}S_8$: Anharmonic Rattling of Interstitial Cu, *Chem. Mater.*, 2021, **33**(8), 2993–3001, DOI: 10.1021/acs.chemmater.1c00659.
15 G. Tan, S. Hao, J. Zhao, C. Wolverton and M. G. Kanatzidis, High Thermoelectric Performance in Electron-Doped $AgBi_3S_5$ with Ultralow Thermal Conductivity, *J. Am. Chem. Soc.*, 2017, **139**(18), 6467–6473, DOI: 10.1021/jacs.7b02399.
16 H. Lin, G. Tan, J. Shen, S. Hao, L. Wu, N. Calta, C. Malliakas, S. Wang, C. Uher, C. Wolverton and M. G. Kanatzidis, Concerted Rattling in $CsAg_5Te_3$ Leading to Ultralow Thermal Conductivity and High Thermoelectric Performance, *Angew. Chem., Int. Ed.*, 2016, **55**(38), 11431–11436, DOI: 10.1002/anie.201605015.
17 S. Mukhopadhyay, D. S. Parker, B. C. Sales, A. A. Puretzky, M. A. McGuire and L. Lindsay, Two-Channel Model for Ultralow Thermal Conductivity of Crystalline Tl_3VSe_4, *Science*, 2018, **360**(6396), 1455–1458, DOI: 10.1126/science.aar8072.
18 S. Mukherjee, D. J. Voneshen, A. Duff, P. Goddard, A. V. Powell and P. Vaqueiro, Beyond Rattling: Tetrahedrites as Incipient Ionic Conductors, *Adv. Mater.*, 2023, **35**(44), 2306088, DOI: 10.1002/adma.202306088.
19 T. Yamada, M. Yoshiya, M. Kanno, H. Takatsu, T. Ikeda, H. Nagai, H. Yamane and H. Kageyama, Correlated Rattling of Sodium-Chains Suppressing Thermal Conduction in Thermoelectric Stannides, *Adv. Mater.*, 2023, **35**(11), 2207646, DOI: 10.1002/adma.202207646.
20 M. Samanta, K. Pal, U. V. Waghmare and K. Biswas, Intrinsically Low Thermal Conductivity and High Carrier Mobility in Dual Topological Quantum Material, n-Type BiTe, *Angew. Chem., Int. Ed.*, 2020, **59**(12), 4822–4829, DOI: 10.1002/anie.202000343.
21 M. Samanta, K. Pal, P. Pal, U. V. Waghmare and K. Biswas, Localized Vibrations of Bi Bilayer Leading to Ultralow Lattice Thermal Conductivity and High Thermoelectric Performance in Weak Topological Insulator *n*-Type BiSe, *J. Am. Chem. Soc.*, 2018, **140**(17), 5866–5872, DOI: 10.1021/jacs.8b02691.
22 M. Samanta, T. Ghosh, S. Chandra and K. Biswas, Layered Materials with 2D Connectivity for Thermoelectric Energy Conversion, *J. Mater. Chem. A*, 2020, **8**(25), 12226–12261, DOI: 10.1039/d0ta00240b.
23 S. Chandra and K. Biswas, Realization of High Thermoelectric Figure of Merit in Solution Synthesized 2D SnSe Nanoplates *via* Ge Alloying, *J. Am. Chem. Soc.*, 2019, **141**(15), 6141–6145, DOI: 10.1021/jacs.9b01396.
24 M. S. Dresselhaus, G. Chen, M. Y. Tang, R. G. Yang, H. Lee, D. Z. Wang, Z. F. Ren, J. -P. Fleurial and P. Gogna, New Directions for Low-Dimensional Thermoelectric Materials, *Adv. Mater.*, 2007, **19**(8), 1043–1053, DOI: 10.1002/adma.200600527.
25 W. G. Zeier, A. Zevalkink, Z. M. Gibbs, G. Hautier, M. G. Kanatzidis and G. J. Snyder, Thinking Like a Chemist: Intuition in Thermoelectric Materials, *Angew. Chem., Int. Ed.*, 2016, **55**(24), 6826–6841, DOI: 10.1002/anie.201508381.
26 Z. Feng, T. Jia, J. Zhang, Y. Wang and Y. Zhang, Dual Effects of Lone-Pair Electrons and Rattling Atoms in $CuBiS_2$ on Its Ultralow Thermal Conductivity, *Phys. Rev. B*, 2017, **96**(23), 235205, DOI: 10.1103/PhysRevB.96.235205.
27 P. Acharyya, T. Ghosh, K. Pal, K. Kundu, K. Singh Rana, J. Pandey, A. Soni, U. V. Waghmare and K. Biswas,

Intrinsically Ultralow Thermal Conductivity in Ruddlesden–Popper 2D Perovskite $Cs_2PbI_2Cl_2$: Localized Anharmonic Vibrations and Dynamic Octahedral Distortions, *J. Am. Chem. Soc.*, 2020, **142**(36), 15595–15603, DOI: 10.1021/jacs.0c08044.

28 D. T. Morelli, V. Jovovic and J. P. Heremans, Intrinsically Minimal Thermal Conductivity in Cubic I − V − VI 2 Semiconductors, *Phys. Rev. Lett.*, 2008, **101**(3), 035901, DOI: 10.1103/PhysRevLett.101.035901.

29 M. D. Nielsen, V. Ozolins and J. P. Heremans, Lone Pair Electrons Minimize Lattice Thermal Conductivity, *Energy Environ. Sci.*, 2013, **6**(2), 570–578, DOI: 10.1039/C2EE23391F.

30 H. Peng, N. Kioussis and G. J. Snyder, Elemental Tellurium as a Chiral p -Type Thermoelectric Material, *Phys. Rev. B:Condens. Matter Mater. Phys.*, 2014, **89**(19), 195206, DOI: 10.1103/PhysRevB.89.195206.

31 D. Sarkar, T. Ghosh, S. Roychowdhury, R. Arora, S. Sajan, G. Sheet, U. V. Waghmare and K. Biswas, Ferroelectric Instability Induced Ultralow Thermal Conductivity and High Thermoelectric Performance in Rhombohedral *p* -Type GeSe Crystal, *J. Am. Chem. Soc.*, 2020, **142**(28), 12237–12244, DOI: 10.1021/jacs.0c03696.

32 A. V. Powell, Recent Developments in Earth-Abundant Copper-Sulfide Thermoelectric Materials, *J. Appl. Phys.*, 2019, **126**(10), 100901, DOI: 10.1063/1.5119345.

33 W. He, D. Wang, H. Wu, Y. Xiao, Y. Zhang, D. He, Y. Feng, Y.-J. Hao, J.-F. Dong, R. Chetty, L. Hao, D. Chen, J. Qin, Q. Yang, X. Li, J.-M. Song, Y. Zhu, W. Xu, C. Niu, X. Li, G. Wang, C. Liu, M. Ohta, S. J. Pennycook, J. He, J.-F. Li and L.-D. Zhao, High Thermoelectric Performance in Low-Cost $SnS_{0.91}Se_{0.09}$ Crystals, *Science*, 2019, **365**(6460), 1418–1424, DOI: 10.1126/science.aax5123.

34 P. Lemoine, G. Guélou, B. Raveau and E. Guilmeau, Crystal Structure Classification of Copper-Based Sulfides as a Tool for the Design of Inorganic Functional Materials, *Angew. Chem., Int. Ed.*, 2022, **61**(2), e202108686, DOI: 10.1002/anie.202108686.

35 G. A. Slack, Nonmetallic crystals with high thermal conductivity, *J. Phys. Chem. Solids*, 1973, **34**(2), 321–335, DOI: 10.1016/0022-3697(73)90092-9.

36 Y.-M. Han, J. Zhao, M. Zhou, X.-X. Jiang, H.-Q. Leng and L.-F. Li, Thermoelectric Performance of SnS and SnS–SnSe Solid Solution, *J. Mater. Chem. A*, 2015, **3**(8), 4555–4559, DOI: 10.1039/C4TA06955B.

37 L.-D. Zhao, B.-P. Zhang, W.-S. Liu, H.-L. Zhang and J.-F. Li, Enhanced Thermoelectric Properties of Bismuth Sulfide Polycrystals Prepared by Mechanical Alloying and Spark Plasma Sintering, *J. Solid State Chem.*, 2008, **181**(12), 3278–3282, DOI: 10.1016/j.jssc.2008.08.022.

38 K. Maji, P. Lemoine, A. Renaud, B. Zhang, X. Zhou, V. Carnevali, C. Candolfi, B. Raveau, R. Al Rahal Al Orabi, M. Fornari, P. Vaqueiro, M. Pasturel, C. Prestipino and E. Guilmeau, A Tunable Structural Family with Ultralow Thermal Conductivity: Copper-Deficient $Cu_{1-x}\square_xPb_{1-x}Bi_{1+x}S_3$, *J. Am. Chem. Soc.*, 2022, **144**(4), 1846–1860, DOI: 10.1021/jacs.1c11998.

39 K. Maji, B. Raveau, S. Fujii, T. Arai, S. Le Tonquesse, C. Prestipino, P. Acharyya, M. Yoshiya and E. Guilmeau, Lone-Pair-Driven Structure Dimensionality: The Way to Ultralow Thermal Conductivity in $Pb_mBi_2S_{3+m}$ Sulfides, *Chem. Mater.*, 2024, **36**(9), 4631–4641, DOI: 10.1021/acs.chemmater.4c00392.

40 P. Acharyya, K. Pal, B. Zhang, T. Barbier, C. Prestipino, P. Boullay, B. Raveau, P. Lemoine, B. Malaman, X. Shen, M. Vaillant, A. Renaud, B. P. Uberuaga, C. Candolfi, X. Zhou and E. Guilmeau, Structure Low Dimensionality and Lone-Pair Stereochemical Activity: The Key to Low Thermal Conductivity in the Pb–Sn–S System, *J. Am. Chem. Soc.*, 2024, **146**(19), 13477–13487, DOI: 10.1021/jacs.4c02893.

41 C. Bourgès, Y. Bouyrie, A. R. Supka, R. Al Rahal Al Orabi, P. Lemoine, O. I. Lebedev, M. Ohta, K. Suekuni, V. Nassif, V. Hardy, R. Daou, Y. Miyazaki, M. Fornari and E. Guilmeau, High-Performance Thermoelectric Bulk Colusite by Process Controlled Structural Disordering, *J. Am. Chem. Soc.*, 2018, **140**(6), 2186–2195, DOI: 10.1021/jacs.7b11224.

42 C. Candolfi, G. Guélou, C. Bourgès, A. R. Supka, R. Al Rahal Al Orabi, M. Fornari, B. Malaman, G. Le Caër, P. Lemoine, V. Hardy, J.-M. Zanotti, R. Chetty, M. Ohta, K. Suekuni and E. Guilmeau, Disorder-Driven Glasslike Thermal Conductivity in Colusite $Cu_{26}V_2Sn_6S_{32}$ Investigated by Mössbauer Spectroscopy and Inelastic Neutron Scattering, *Phys. Rev. Mater.*, 2020, **4**(2), 025404, DOI: 10.1103/PhysRevMaterials.4.025404.

43 K. Maji, B. Raveau, P. Lemoine, P. Boullay, P. Acharyya, X. Shen, A. Renaud, V. Pelletier, R. Gautier, V. Carnevali, M. Fornari, B. Zhang, X. Zhou, B. Lenoir, C. Candolfi and E. Guilmeau, Three-Fold Coordination of Copper in Sulfides: A Blockade for Hole Carrier Delocalization but a Driving Force for Ultralow Thermal Conductivity, *J. Am. Chem. Soc.*, 2024, **146**(14), 9741–9754, DOI: 10.1021/jacs.3c13884.

44 C. Bourgès, P. Lemoine, O. I. Lebedev, R. Daou, V. Hardy, B. Malaman and E. Guilmeau, Low Thermal Conductivity in Ternary $Cu_4Sn_7S_{16}$ Compound, *Acta Mater.*, 2015, **97**, 180–190, DOI: 10.1016/j.actamat.2015.06.046.

45 K. Suekuni, K. Tsuruta, M. Kunii, H. Nishiate, E. Nishibori, S. Maki, M. Ohta, A. Yamamoto and M. Koyano, High-Performance Thermoelectric Mineral $Cu_{12-x}Ni_xSb_4S_{13}$ Tetrahedrite, *J. Appl. Phys.*, 2013, **113**(4), 043712, DOI: 10.1063/1.4789389.

46 Z. Li, Z. Zhou, J. Zhang, C. Zhu, P. Qiu, T. Deng, F. Xu, L. Chen and X. Shi, Intrinsically Low Thermal Conductivity in a Novel Cu-S Modified ZrS_2 Compound with Asymmetric Bonding, *Small*, 2023, **19**(52), 2304718, DOI: 10.1002/smll.202304718.

47 E. Rathore, R. Juneja, S. P. Culver, N. Minafra, A. K. Singh, W. G. Zeier and K. Biswas, Origin of Ultralow Thermal Conductivity in N-Type Cubic Bulk $AgBiS_2$: Soft Ag Vibrations and Local Structural Distortion Induced by the Bi $6s^2$ Lone Pair, *Chem. Mater.*, 2019, **31**(6), 2106–2113, DOI: 10.1021/acs.chemmater.9b00001.

48 V. P. Kumar, P. Lemoine, V. Carnevali, G. Guélou, O. I. Lebedev, B. Raveau, R. Al Rahal Al Orabi, M. Fornari, C. Candolfi, C. Prestipino, D. Menut, B. Malaman, J. Juraszek, K. Suekuni and E. Guilmeau, Local-Disorder-Induced Low Thermal Conductivity in Degenerate Semiconductor $Cu_{22}Sn_{10}S_{32}$, *Inorg. Chem.*, 2021, **60**(21), 16273–16285, DOI: 10.1021/acs.inorgchem.1c02105.

49 K. K. Joshi, P. M. Pataniya, G. R. Bhadu and C. K. Sumesh, Cu_2CoSnS_4 Electrocatalyst Embedded Paper Working Electrodes for Efficient, Stable, pH Universal, and Large-Current-Density Hydrogen Evolution Reaction, *Int. J. Hydrogen Energy*, 2024, **49**, 829–842, DOI: 10.1016/j.ijhydene.2023.09.185.

50 Y. Shen, C. Li, R. Huang, R. Tian, Y. Ye, L. Pan, K. Koumoto, R. Zhang, C. Wan and Y. Wang, Eco-Friendly p-Type Cu_2SnS_3 Thermoelectric Material: Crystal Structure and Transport Properties, *Sci. Rep.*, 2016, **6**(1), 32501, DOI: 10.1038/srep32501.

51 L. Le Gars, M. Tiadi, S. Le Tonquesse, B. Zhang, T. C. Tran, Y. Kim, C. Kim, M. Yoshiya, S. Fujii, C. Prestipino, E. Elkaïm, P. Lemoine, B. Raveau, K. Suekuni, B. Malaman, G. Le Caër, T. Schweitzer, C. Candolfi, A. Renaud, X. Zhou and E. Guilmeau, Coexistence of Two Sphalerite Frameworks: A Vector for the Enhancement of Thermoelectric Performances in Zn-Doped $Cu_5Sn_2S_7$, *Chem. Mater.*, 2025, **37**(14), 5271–5285, DOI: 10.1021/acs.chemmater.5c00972.

52 S. Tippireddy, F. Azough, F. T. Tompkins, A. Bhui, R. Freer, R. Grau-Crespo, K. Biswas, P. Vaqueiro and A. V. Powell, Tin-Substituted Chalcopyrite: An *n* -Type Sulfide with Enhanced Thermoelectric Performance, *Chem. Mater.*, 2022, **34**(13), 5860–5873, DOI: 10.1021/acs.chemmater.2c00637.

53 J. D. Burnett, O. Gourdon, K. G. S. Ranmohotti, N. J. Takas, H. Djieutedjeu, P. F. P. Poudeu and J. A. Aitken, Structure–Property Relationships along the Fe-Substituted $CuInS_2$ Series: Tuning of Thermoelectric and Magnetic Properties, *Mater. Chem. Phys.*, 2014, **147**(1–2), 17–27, DOI: 10.1016/j.matchemphys.2014.03.034.

54 V. Petříček, M. Dušek and L. Palatinus, Crystallographic Computing System JANA2006: General Features, *Z. Kristallogr. Cryst. Mater.*, 2014, **229**(5), 345–352, DOI: 10.1515/zkri-2014-1737.

55 L. Palatinus and G. Chapuis, *SUPERFLIP* – a Computer Program for the Solution of Crystal Structures by Charge Flipping in Arbitrary Dimensions, *J. Appl. Crystallogr.*, 2007, **40**(4), 786–790, DOI: 10.1107/S0021889807029238.

56 B. Sitaud, P. L. Solari, S. Schlutig, I. Llorens and H. Hermange, Characterization of Radioactive Materials Using the MARS Beamline at the Synchrotron SOLEIL, *J. Nucl. Mater.*, 2012, **425**(1–3), 238–243, DOI: 10.1016/j.jnucmat.2011.08.017.

57 J. Rodríguez-Carvajal, Recent Advances in Magnetic Structure Determination by Neutron Powder Diffraction, *Phys. B*, 1993, **192**(1–2), 55–69, DOI: 10.1016/0921-4526(93)90108-I.

58 T. Roisnel, WinPLOTR: A Windows Tool for Powder Diffraction Pattern Analysis, *Mater. Sci. Forum*, 2001, **378–381**, 118–123, DOI: 10.4028/www.scientific.net/MSF.378-381.118.

59 M. Casas-Cabanas, M. Reynaud, J. Rikarte, P. Horbach and J. Rodríguez-Carvajal, *FAULTS* : A Program for Refinement of Structures with Extended Defects, *J. Appl. Crystallogr.*, 2016, **49**(6), 2259–2269, DOI: 10.1107/S1600576716014473.

60 M. Gemmi, E. Mugnaioli, T. E. Gorelik, U. Kolb, L. Palatinus, P. Boullay, S. Hovmöller and J. P. Abrahams, 3D Electron Diffraction: The Nanocrystallography Revolution, *ACS Cent. Sci.*, 2019, **5**(8), 1315–1329, DOI: 10.1021/acscentsci.9b00394.

61 S. Smeets, B. Wang and E. Hogenbirk, *Instamatic-Dev/Instamatic: 1.7.0*, 2021, DOI: 10.5281/ZENODO.5175957.

62 L. Palatinus, P. Brázda, M. Jelínek, J. Hrdá, G. Steciuk and M. Klementová, Specifics of the Data Processing of Precession Electron Diffraction Tomography Data and Their Implementation in the Program *PETS2.0*, *Acta Crystallogr., Sect. B:Struct. Sci., Cryst. Eng. Mater.*, 2019, **75**(4), 512–522, DOI: 10.1107/S2052520619007534.

63 V. Petříček, L. Palatinus, J. Plášil and M. Dušek, Jana2020 – a New Version of the Crystallographic Computing System Jana, *Z. Kristallogr. Cryst. Mater.*, 2023, **238**(7–8), 271–282, DOI: 10.1515/zkri-2023-0005.

64 E. Alleno, D. Bérardan, C. Byl, C. Candolfi, R. Daou, R. Decourt, E. Guilmeau, S. Hébert, J. Hejtmanek, B. Lenoir, P. Masschelein, V. Ohorodnichuk, M. Pollet, S. Populoh, D. Ravot, O. Rouleau and M. Soulier, Invited Article: A Round Robin Test of the Uncertainty on the Measurement of the Thermoelectric Dimensionless Figure of Merit of $Co_{0.97}Ni_{0.03}Sb_3$, *Rev. Sci. Instrum.*, 2015, **86**(1), 011301, DOI: 10.1063/1.4905250.

65 G. Kresse and J. Hafner, *Ab Initio* Molecular Dynamics for Liquid Metals, *Phys. Rev. B:Condens. Matter Mater. Phys.*, 1993, **47**(1), 558–561, DOI: 10.1103/PhysRevB.47.558.

66 G. Kresse and J. Furthmüller, Efficiency of Ab-Initio Total Energy Calculations for Metals and Semiconductors Using a Plane-Wave Basis Set, *Comput. Mater. Sci.*, 1996, **6**(1), 15–50, DOI: 10.1016/0927-0256(96)00008-0.

67 G. Kresse and J. Furthmüller, Efficient Iterative Schemes for *Ab Initio* Total-Energy Calculations Using a Plane-Wave Basis Set, *Phys. Rev. B:Condens. Matter Mater. Phys.*, 1996, **54**(16), 11169–11186, DOI: 10.1103/PhysRevB.54.11169.

68 J. P. Perdew, A. Ruzsinszky, G. I. Csonka, O. A. Vydrov, G. E. Scuseria, L. A. Constantin, X. Zhou and K. Burke, Restoring the Density-Gradient Expansion for Exchange in Solids and Surfaces, *Phys. Rev. Lett.*, 2008, **100**(13), 136406, DOI: 10.1103/PhysRevLett.100.136406.

69 A. Togo, L. Chaput, T. Tadano and I. Tanaka, Implementation Strategies in Phonopy and Phono3py, *J. Phys.: Condens. Matter*, 2023, **35**(35), 353001, DOI: 10.1088/1361-648X/acd831.

70 A. Togo, First-Principles Phonon Calculations with Phonopy and Phono3py, *J. Phys. Soc. Jpn.*, 2023, **92**(1), 012001, DOI: 10.7566/JPSJ.92.012001.

71 J. P. Dismukes, R. T. Smith and J. G. White, Physical Properties and Crystal Structure of a New Semiconducting

I–III–VI2 Compound, CuScS2, *J. Phys. Chem. Solids*, 1971, **32**(5), 913–922, DOI: 10.1016/S0022-3697(71)80336-0.

72 G. C. Tewari, M. Karppinen and A. K. Rastogi, Effects of Competing Magnetic Interactions on the Electronic Transport Properties of CuCrSe2, *J. Solid State Chem.*, 2013, **198**, 108–113, DOI: 10.1016/j.jssc.2012.09.033.

73 M. M. J. Treacy, J. M. Newsam and M. W. Deem, A General Recursion Method for Calculating Diffracted Intensities from Crystals Containing Planar Faults, *Proc. R. Soc. London, Ser. A*, 1991, **433**(1889), 499–520, DOI: 10.1098/rspa.1991.0062.

74 B. Di Bartolo, *Optical Interactions in Solids*, World Scientific Publishing Company, 2010.

75 L. Bergman, D. Alexson, P. L. Murphy, R. J. Nemanich, M. Dutta, M. A. Stroscio, C. Balkas, H. Shin and R. F. Davis, Raman Analysis of Phonon Lifetimes in AlN and GaN of Wurtzite Structure, *Phys. Rev. B:Condens. Matter Mater. Phys.*, 1999, **59**(20), 12977.

76 M. Alam, K. H. Gooen, B. D. Bartolo, A. Linz, E. Sharp, L. Gillespie and G. Janney, Optical Spectra and Laser Action of Neodymium in a Crystal $Ba_2MgGe_2O_7$, *J. Appl. Phys.*, 1968, **39**(10), 4728–4730.

77 P. G. Klemens, Anharmonic Decay of Optical Phonons, *Phys. Rev.*, 1966, **148**(2), 845–848, DOI: 10.1103/PhysRev.148.845.

78 M. Balkanski, R. F. Wallis and E. Haro, Anharmonic Effects in Light Scattering Due to Optical Phonons in Silicon, *Phys. Rev. B:Condens. Matter Mater. Phys.*, 1983, **28**(4), 1928–1934, DOI: 10.1103/PhysRevB.28.1928.

79 H.-S. Kim, Z. M. Gibbs, Y. Tang, H. Wang and G. J. Snyder, Characterization of Lorenz Number with Seebeck Coefficient Measurement, *APL Mater.*, 2015, **3**(4), 041506, DOI: 10.1063/1.4908244.

80 I. K. Dimitrov, M. E. Manley, S. M. Shapiro, J. Yang, W. Zhang, L. D. Chen, Q. Jie, G. Ehlers, A. Podlesnyak, J. Camacho and Q. Li, Einstein Modes in the Phonon Density of States of the Single-Filled Skutterudite $Yb_{0.2}Co_4Sb_{12}$, *Phys. Rev. B:Condens. Matter Mater. Phys.*, 2010, **82**(17), 174301, DOI: 10.1103/PhysRevB.82.174301.

81 Y. Xiao, C. Chang, Y. Pei, D. Wu, K. Peng, X. Zhou, S. Gong, J. He, Y. Zhang, Z. Zeng and L.-D. Zhao, Origin of Low Thermal Conductivity in SnSe, *Phys. Rev. B:Condens. Matter Mater. Phys.*, 2016, **94**(12), 125203, DOI: 10.1103/PhysRevB.94.125203.

82 Y.-X. Zhang, Q.-Y. Huang, X. Yan, C.-Y. Wang, T.-Y. Yang, Z.-Y. Wang, Y.-C. Shi, Q. Shan, J. Feng and Z.-H. Ge, Synergistically Optimized Electron and Phonon Transport in High-Performance Copper Sulfides Thermoelectric Materials *via* One-Pot Modulation, *Nat. Commun.*, 2024, **15**(1), 2736, DOI: 10.1038/s41467-024-47148-0.

83 J. Callaway, Model for Lattice Thermal Conductivity at Low Temperatures, *Phys. Rev.*, 1959, **113**(4), 1046–1051, DOI: 10.1103/PhysRev.113.1046.

84 C. J. Glassbrenner and G. A. Slack, Thermal Conductivity of Silicon and Germanium from 3°K to the Melting Point, *Phys. Rev.*, 1964, **134**(4A), A1058–A1069, DOI: 10.1103/PhysRev.134.A1058.

85 X. Shi, Y. Pei, G. J. Snyder and L. Chen, Optimized Thermoelectric Properties of $Mo_3Sb_{7-x}Te_x$ with Significant Phonon Scattering by Electrons, *Energy Environ. Sci.*, 2011, **4**(10), 4086, DOI: 10.1039/c1ee01406d.

86 M. G. Holland, Analysis of Lattice Thermal Conductivity, *Phys. Rev.*, 1963, **132**(6), 2461–2471, DOI: 10.1103/PhysRev.132.2461.

87 M. Jin, J. Liang, P. Qiu, H. Huang, Z. Yue, L. Zhou, R. Li, L. Chen and X. Shi, Investigation on Low-Temperature Thermoelectric Properties of Ag_2Se Polycrystal Fabricated by Using Zone-Melting Method, *J. Phys. Chem. Lett.*, 2021, **12**(34), 8246–8255, DOI: 10.1021/acs.jpclett.1c02139.

